SEISMIC IMAGING OF ACTIVE AND ANCIENT CO2 PATHWAYS IN THE LITTLE GRAND WASH FAULT

by

Jonathan Yelton

A thesis

submitted in partial fulfillment

of the requirements for the degree of

Master of Science in Geophysics

Boise State University

August 2021

BOISE STATE UNIVERSITY GRADUATE COLLEGE

DEFENSE COMMITTEE AND FINAL READING APPROVALS

of the thesis submitted by

Jonathan Yelton

Thesis Title: Seismic Imaging of Active and Ancient CO2 Pathways in the Little Grand Wash Fault

Date of Final Oral Examination: 14 July 2021

The following individuals read and discussed the thesis submitted by student Jonathan Yelton, and they evaluated the student's presentation and response to questions during the final oral examination. They found that the student passed the final oral examination.

Lee Liberty, M.S.	Chair, Supervisory Committee
Dylan Mikesell, Ph.D.	Member, Supervisory Committee
Qifei Niu, Ph.D.	Member, Supervisory Committee

The final reading approval of the thesis was granted by Lee Liberty, M.S, Chair of the Supervisory Committee. The thesis was approved by the Graduate College.

DEDICATION

I would like to dedicate this to my wife Kirstie, who made the sacrifice to move across the country and help me while I pursued my education. Her love and support are invaluable to me and has made this all possible, thank you.

ACKNOWLEDGMENTS

I want to acknowledge James St. Clair, Tom Otheim, William Schermerhorn, and Steve Slivicki who worked with me on field trips to collect my data.

I want to thank the members of my committee and give a special thanks to my advisor Lee Liberty who gave me the opportunity to pursue higher education at Boise State University and helped every step along the way.

Finally, I would like to thank my friends in Boise, Idaho who made graduate school less stressful and provided a feeling of community for me.

ABSTRACT

Understanding the migration behavior of carbon dioxide (CO_2) during long-term geological storage is crucial to the success of carbon capture and sequestration technology. I explore p-wave and s-wave seismic properties across the Little Grand Wash fault in east-central Utah, a natural CO_2 seep and analogue for a long-failed sequestration site. Travertines dated to at least 113,000 k.y. and geochemical surveys confirm both modern and ancient CO_2 leakage along the fault. Outgassing is currently focused in damage zones where the total fluid pressure may reduce the minimum horizontal effective stress. Regional stress changes may be responsible for decadal- to millennial-scale changes in CO_2 pathways.

I identify subsurface geologic structure in the upper few hundred meters and relate surface CO_2 outgassing zones to seismic reflection and first arrival tomography data. I tie my hammer seismic results to borehole logs, geology from outcrops, and geochemical data. I generate velocity tomograms that cross the fault zone and construct rock physics models. I identify high porosity and/or high fracture density zones from slow seismic velocity zones. These zones match mapped fault locations, are fully saturated, and are conduits for upward fluid/gas migration. Anomalously high seismic velocities at the fault are consistent with ancient CO_2 flow pathways. Low CO_2 flux regions show seismic velocities consistent with shallow unsaturated host rock. Studying the behavior of CO_2 in this system can give insight of potential risks in future sequestration projects.

TABLE OF CONTENTS

LIST OF TABLES

LIST OF FIGURES

LIST OF ABBREVIATIONS

BSU	Boise State University
CO2	Carbon Dioxide
CSS	Carbon Storage and Sequestration
LGWF	Little Grand Wash Fault
CG	Crystal Geyser
BGL	Below Ground Level
SWG	Salt Wash Graben

CHAPTER ONE: INTRODUCTION

Importance of Research

Anthropogenic carbon dioxide (CO_2) release into the atmosphere presents a threat to human civilization in the form of climate change. CO_2 constitutes approximately 77% of greenhouse gases in the atmosphere and carbon emissions increased annually at a rate of roughly 1% from 1990 to 2007 (Rahman et al., 2017). Although CO_2 emissions have been decreasing about 1.5 % annually since 2007, the total amount of CO_2 in the atmosphere continues to rise. Data from the National Oceanic and Atmospheric Administration (NOAA) National Center for Environmental Information showed an average CO_2 concentration of 409.8 ppm in 2019, the highest level in the last 800,000 years (Lindsey, 2020). Climate models predict a rise in global temperature of between 1.9 and 5.0 degrees Celsius by the end of the 21^{st} century (O'Neill et al., 2016).

One practical strategy to reduce atmospheric CO_2 introduced by human activity is carbon capture and sequestration (CCS). CSS is the process by which CO_2 from power plants, refineries or other industrial sources is compressed, transported, and injected into a subsurface reservoir for long term storage (Figure 1.1). The storage of CO_2 in subsurface reservoirs is generally believed to be one of the most effective ways to address global warming by reducing carbon emissions into the atmosphere (Chu, 2009). According to the International Panel on Climate Change (IPCC), to achieve the recommended limiting average warming of the atmosphere to <2°C, roughly 10 Gt CO_2 per year must be sequestered by 2050 (Kelemen et al., 2019). The 2019 report from the Global CCS Institute states that currently operational and under construction facilities have the capacity to store 40 Mt per year.

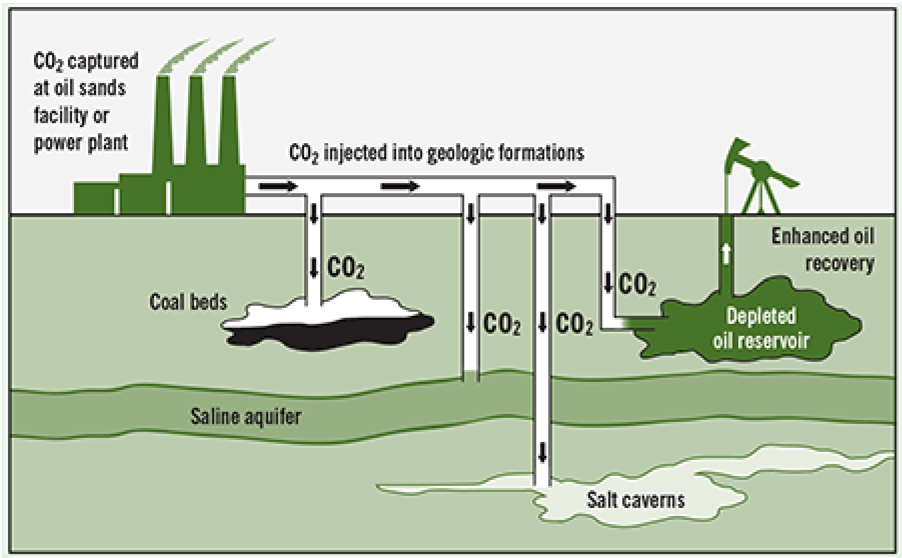

Figure 1.0 Schematic of Carbon Capture and Sequestration process in geological storage reservoirs.

Assessing reservoir integrity and predicting post-injection CO2 migration behavior is vital to the success of CCS projects. A major component to predicting subsurface CO2 migration is determining how pre-existing faults or other permeable pathways within the reservoir may enhance or restrict flow both laterally and vertically. Relevant questions are: 1) will mineral precipitation “self-seal” pathways via carbonate veining? 2) will increased injection pressure open fractures in the fault damage zone, permitting more CO2 flow? and 3) at what rate will CO2 leak back to the surface, thus reducing CCS effectiveness?

To date, small or short-term CCS operations have been inadequate to predict the behavior of stored CO2 at the thousand-year time scale. To explore the potential leakage of CO2 via permeable pathways back to the atmosphere, I characterize the regolith and underlying rock properties across naturally occurring CO2 seeps. I utilize seismology because it is the best imaging tool to remotely sense mechanical properties of soils and rock. From this information, I can estimate porosity and fluid saturation distributions that promote or inhibit CO2 flow.

I acquired eight parallel seismic profiles spanning three km of the Little Grand Wash fault (LGWF). Here, the fault and underlying Green River anticline provide a trap and conduit for CO2 that outgasses to the surface (Jung, 2014). My surveys were conducted in October, 2019 and January, 2020. From these data, I identify a fault damage zone, underlying stratigraphy and structure, and interpret rock, fluid, gas, and regolith distributions from velocity variance in the upper tens of meters. I also provide empirical estimates of seismic velocity ranges for different lithologies and in the presence or absence of fluid saturation (Mavko et al., 2020). My seismic results validate the low seismic velocity/high porosity relationship for the established pathways where reservoir CO2 degasses along the fault; and conversely, the high velocity/low porosity zones where low CO2 flux rates have been measured.

In this thesis, I first provide a rock physics framework for soils and shallow rocks within my study area. I then describe the geologic and tectonic setting of east-central Utah, with details on the LGWF and the related CO2 brine system. I describe the seismic methods that I use to characterize the fault system, followed by detailed interpretations from each seismic profile. Then I connect my interpretations to effects of fluid and CO2 gas on rock properties and seismic velocities within the fault damage zone to remotely characterize and ancient CO2 pathways from surface measurements. Finally, I place my results in the context of CCS technology and provide future directions that may stem from my research.

Rock Properties and Effects on Seismic Velocities

Seismic velocities directly relate to elastic moduli and bulk density of a material. For soils and rock, influences on seismic velocity include effective pressure, pore pressure, lithology, grain shape, porosity (ϕ), and the fluid or gas that occupies the pore space. Host rock can be damaged through accumulation and release of strain through faulting. Faults that extend to the earth's surface can produce a broad damage zone. Within this damage zone, relatively low ϕ host rock can transform to high ϕ sediments. These high ϕ sediments often produce high permeability conditions (e.g., Caine et al., 1996), allowing CCS stored CO2 to release back into the atmosphere. Within a fault's damage zone, seismic velocities generally decrease due to a decrease in elastic moduli. Thus, seismic velocity mapping is a viable approach to identifying high permeability damage zones that may provide fluid and gas release to the earth surface (Gettemy et al., 2004).

For sedimentary rock environments where surface rupturing faults are present, advective flow dominates gas migration through groundwater. Here, two conditions must be present for a fault to behave as a conduit for CO2 surface outgassing. First, the pore fluid pressure must reduce the effective stress to approximately zero (Naruk et al., 2019). Second, there must be pre-existing high porosity fractures within the fault's damage zone. In other words, mineral precipitation or cementation within the fault zone, and diffusive flow through the soils, is negligible.

There are three main factors that influence permeability within a fault zone (e.g., Faulkner et al., 2010). The first factor is the porosity of the host rock matrix. Higher porosity rock tends to have more interconnected pore space and therefore higher permeability that can extend in all directions. The second factor is fracture related porosity. For example, the connectivity of a fracture network in the damage zone of a fault can provide more pathways for fluids and increase permeability. Generally, a higher fracture density means more vertically connected fracture pathways and therefore higher permeability in the fault zone. The third factor is the porosity of the fault core matrix. When fault movement occurs, it can break the host rock into rock clasts and gouge. The resulting matrix can either increase or decrease permeability that is controlled mostly by porosity distributions. Since faults generally form at high angles to the earth's surface, these permeability effects can strongly influence vertical fluid flow. The interplay between these three factors determine how fluid may move vertically and horizontally within a fault zone. To investigate the degree of impact these factors have on fluid and gas flow within the LGWF, I use p-wave velocities (Vp) to estimate ϕ and fracture density within the bedrock from previously established relationships. From Vp and an independent measure of CO2 outgassing, I infer the permeability of along seismic profiles that cross the LGWF.

I estimate porosity based on Vp from my tomographic results. I use the Castagna et al. (1985) relationships to estimate ϕ from seismic velocity (Figure 1.1). As shown in Brocher et al. (2005), these relationships have a high correlation for sedimentary rocks in the Vp range of 1500 to 4500 m/s. Because I generate only Vp models for all seismic profiles, I use their empirically derived Vp/porosity relationship from the Frio sandstone (Equation 1). I assume a formation clay content of 20% (V_{cl}) (Dockrill and Shipton, 2010) for fully saturated conditions, consistent with the Entrada Sandstone. Unaltered Entrada sandstone shows ϕ of about 25% at reservoir depths (Ridgley and Hatch, 2013).

This unit is found near the surface and within the footwall of the LGWF. Although I acknowledge that an estimate of absolute ϕ requires direct sample measurements, I rely on my ϕ estimates to identify relative changes that may relate to high permeability CO_2/fluid pathways. For the one profile where I measure both Vp and shear wave velocities (Vs), I compare two additional velocity/porosity Castagna et al. (1985) empirical relationships. These are as follows:

$$V_p = 5.81 - 9.42 * \phi - 2.21 * V_{cl} \quad (1)$$

$$V_s = 3.89 - 7.07 * \phi - 2.04 * V_{cl} \quad (2)$$

$$\frac{V_p}{V_s} = 1.33 + .63 * (3.89 - 7.07 * \phi) \quad (3)$$

For these equations, Vp and Vs are measured in km/s. Using the above equations with $\phi = 0.25$ and $V_{cl} = 0.20$, I calculate Vp~3.0 km/s, Vs~1.7 km/s, and Vp/Vs~1.76 for unaltered sandstone. The velocities will be reduced in the presence of increasing clay content and ϕ, as may be expected within the fault's damage zone

Effective stress or effective pressure on a fault system can directly influence seismic velocity. Increasing effective pressure by burial or other tectonic processes can close pre-existing microfractures, flaws, and grain boundaries, thus increasing rock stiffness and seismic velocity (Mavko et al., 2020). Closing of micro fractures in a damage zone associated with high effective pressure lowers overall porosity and reduces pore to pore connections which decreases permeability. A fault system under high effective pressure will likely act as a barrier to fluid or CO_2 migration.

Pore pressure is the other side of the push and pull of overall stress within the fault zone. Increasing pore fluid pressure can act to open pre-existing fractures and reduce the effects of effective stress. High pore pressure acts to open micro fractures, flaws and grain boundaries, increasing what is termed soft porosity i.e., the aspect of porosity that changes with changing pressure regime. A combination of high pore pressure and low effective pressure within the fault damage zone can increase soft porosity, thereby reducing seismic velocities. In contrast, diagenesis can increase seismic velocities as cementation can increase the soil or rock's elastic properties. High pore pressure persisting over long periods of time can inhibit diagenesis and preserve porosity, tending to keep velocities low (Mavko et al., 2020). These open pathways will show a decrease in seismic velocity and likely act as a conduit to upward fluid or CO_2 migration.

Whereas Vp is sensitive to bulk (k) and shear (μ) moduli, shown also as Lame parameters (λ) and (μ), and bulk density (ρ) (Equation 4), Vs is insensitive to λ and driven only by μ and ρ (Equation 5). Seismic velocity equations are shown for p-waves (Equation 4), and shear waves (Equation 5), where μ, and, ρ are bulk modulus, shear modulus, and density of the formation, respectively.

$$\boxed{V_P = \sqrt{\frac{k + 4/3\,\mu}{\rho}} = \sqrt{\frac{\lambda + 2\mu}{\rho}}} \qquad (4)$$

$$\boxed{V_S = \sqrt{\frac{\mu}{\rho}}} \qquad (5)$$

The presence of fluid within soils can strongly influence Vp (Figure 1.1) by increasing the bulk modulus more than the bulk density (Mavko et al., 2020). Fluid changes in a soil or rock do not significantly influence Vs since shear waves do not propagates through fluids. The bulk modulus always increases with a less compressible pore fluid, and the velocity change is most effective on soft (low velocity) rock or soil. Pore pressure from saturation can also open fractures and grain boundaries within the damage zone increasing porosity, reducing grain-to-grain contacts and thereby decreasing velocity.

Clark and Burbank (2011) derived an equation to estimate fracture density (P_f) from the measured velocity (V), the velocity derived from unaltered rock (V_r), and the velocity of the fracture filling material (V_f).

$$P_f = \frac{V_f}{(V_r - V_f)}\left(\frac{V_r}{V} - 1\right) \tag{6}$$

measured velocity (V)
intact rock velocity (Vr)
velocity of the fracture-filling material (Vf)
fracture density (Pf)

Assumptions to satisfy this equation include a single material filling the void space (e.g., water or air) and that the seismic rays propagate laterally through the fractures (e.g., vertical fractures and horizontally traveling seismic ray paths). In my case, I assume full saturation and pore space filled with water or $V_f = 1.5$ km/s (e.g., Mavko et al., 2020). I assume that V_r is best represented by the maximum velocity in my tomogram. The assumption of horizontal ray paths and vertical fractures is valid for materials below the near surface and for this tectonic environment. Here, rays will bend toward the surface within the regolith or where weathered rock is present, and high angle faults have been mapped (e.g., Dockrill and Shipton, 2010). To focus on horizontal ray path coverage, I exclude the regions where $Vp < 2.0$ km/s. Below this velocity, rock physics models suggest the presence of unsaturated unconsolidated material (Figure 1.1).

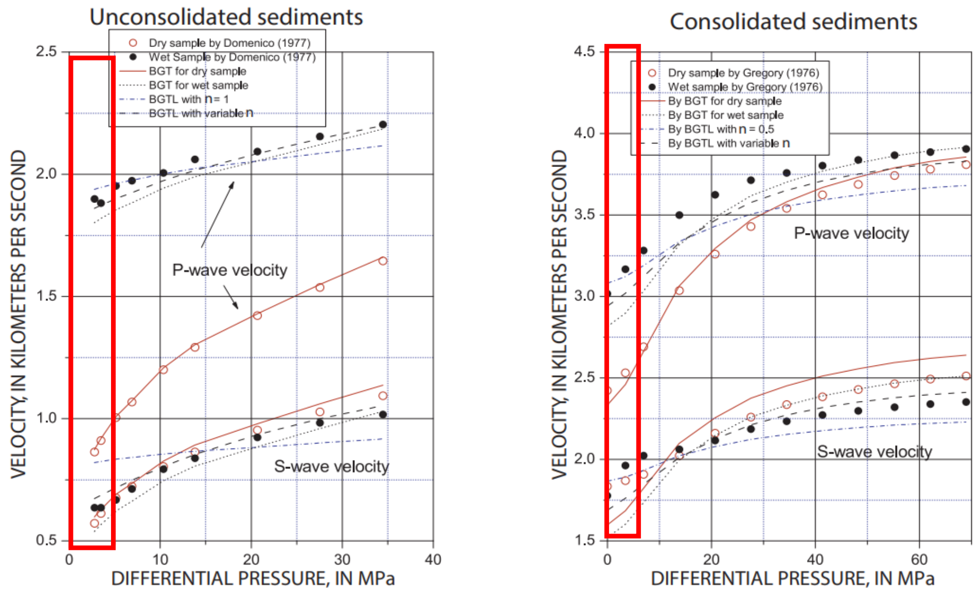

Figure 1.1 Relationships of Vp and Vs to differential pressure in saturated and unsaturated unconsolidated sediments (left) and saturated and unsaturated consolidated sediments (right). I focus on the pressure range of 0 to 5 MPa for my study.

Although gas can influence seismic velocity, CO2 concentration has little effect on Vp within unsaturated materials. This results from the ρ and Vp of CO2 being similar to that of air. Results of laboratory experiments on saturated Berea sandstone samples indicate a 5.4% Vp velocity reduction at 25% CO2 concentration that plateaus at higher CO2 concentrations (Gutierrez et al., 2012). Numerical simulations by Yamabe et al. (2016) predict a 9% Vp decrease at full saturation of CO2 (equilibrium state). Given that my model uncertainties are similar to the expected velocity changes from gas content, I focus my interpretations only on fluid, soil and rock properties. My study area consists of sandstones and shales that have weathered to regolith and soils. The Green River lies within my study area, generally providing saturation at or below river elevations.

CHAPTER TWO: GEOLOGIC SETTING

Regional Geology

The Paradox Basin, located in eastern Utah, is an oval shaped paleotectonic depression of Late Paleozoic age (Figure 2.0; Nuccio et al., 2000). The basin boundaries are defined by the extent of salt deposited during Middle Pennsylvanian Paradox sediment formation. This unit consists of carbonate, halite, and clasitcs that responded to tectonic stresses and the simultaneous uplift along its northeastern border. The shape of the basin was modified by later tectonic events affiliated with the Cretaceous and younger Laramide orogeny. Today, the basin has been dissected in places by uplift of the Colorado Plateau and downcutting by the Colorado River and its tributaries.

Little Grand Wash Fault

The LGWF is an east-west trending south-dipping normal fault located on the northwest margin of the Paradox Basin near Green River, east-central Utah (Figure 2.0). The fault has a ~30km arcuate surface expression (Dockrill and Shipton, 2010), and the central span intersects with the crest of the Green River Anticline. Within the central span, the fault becomes a more segmented fault zone with two dominant fault traces, accompanied by a series of minor faults and relay ramps (Oye et al., 2021). Fault throw is greatest at 250-300 meters in the central span of the fault near the Green River and juxtaposes Jurassic Morrison Formation and Cretaceous Mancos Shale (Kampman et al., 2014). Among the northern and southern fault traces, the southern fault accounts for approximately 215 meters of throw. From outcrops, previous field mapping studies found the fault to have a core of 0.7-to-3-meter foliated clay-rich gouge with ~1 m of highly fractured damage zone (Jung, 2014, Dockrill and Shipton, 2010). Further fracturing that extends 20-30 m from the fault was also identified by Dockrill and Shipton (2010). According to Caine et al. (1996), a combination of low percentage fault core and high percentage damage zone suggests the fault would act as a diffusive conduit for vertical fluid flow. Timing of continued movement along the LGWF is poorly constrained, though thought to be Tertiary and younger slip (Shipton et al., 2004). Modern seismicity along the LGWF has been inferred from earthquakes with hypocenters within three km of Crystal geyser in 2006 and 2010 (Han et al., 2013). The respective magnitudes of the earthquakes were 1.17 and 2.63. Han et al. (2013) also hypothesized that these two events could have initiated movement of the Little Grand Wash fault system and disturbed the eruption patterns of Crystal Geyser.

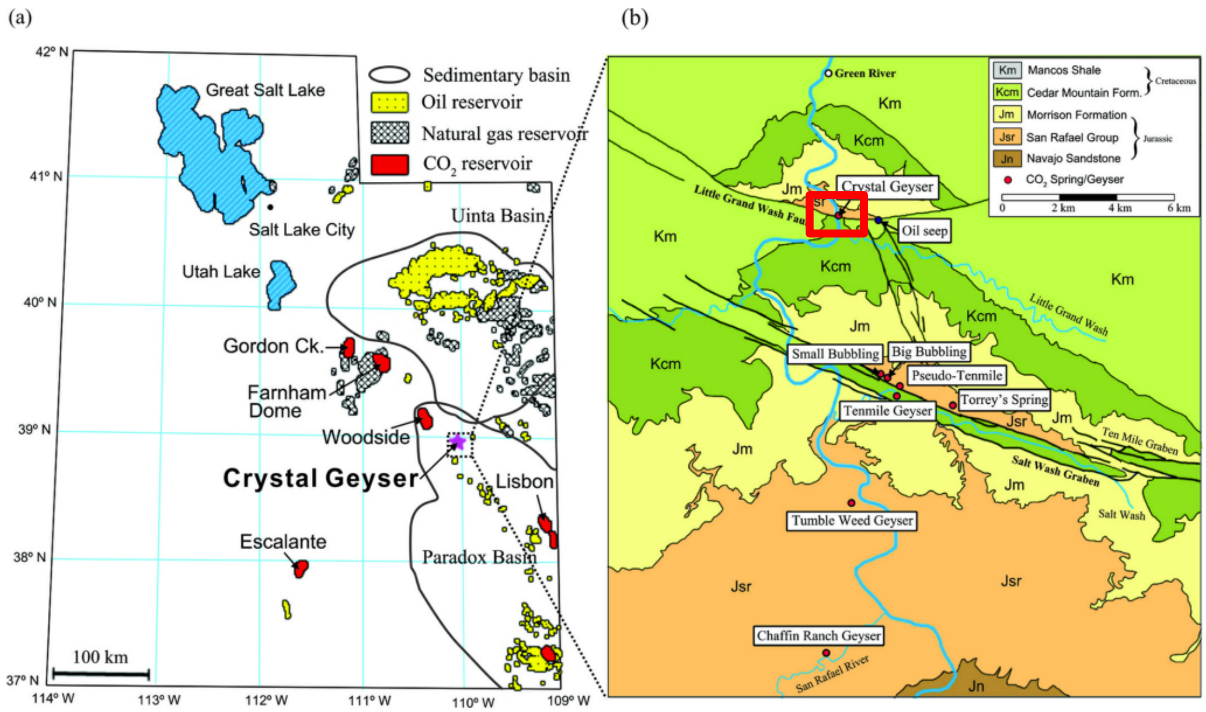

Figure 2.0 Map of regional geological basins (a) as well as known oil, natural gas, and CO2 reservoirs. Simplified geological map (b) of the LGWF and SWG with local springs and geysers. The approximate study area in detail (Figure 2.1) is shown as a red square. Figure modified from Jung (2014).

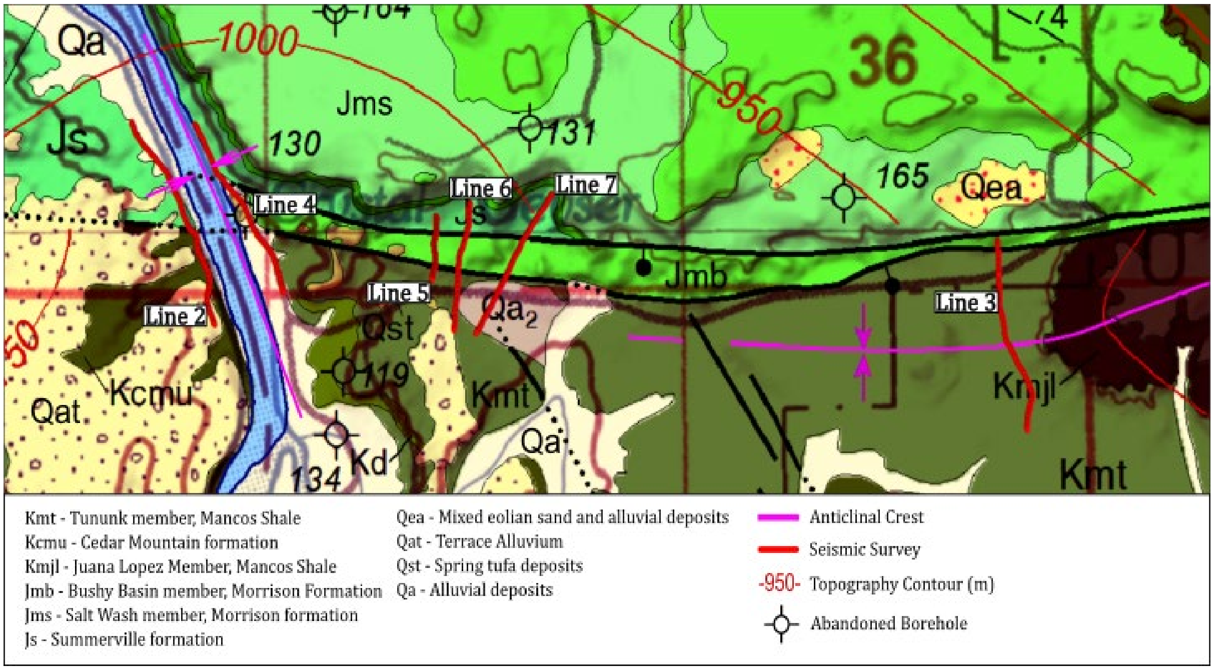

Figure 2.1 Geological map by Doelling et al. (2015) of the LGWF near Crystal Geyser. Shown also are seismic profiles (in red), local anticlines (purple), and abandoned boreholes. The red contours represent structure contours, in meters, drawn on top of Navajo Sandstone above mean sea level.

To the south of both fault strands of the LGWF, or within the fault's hanging wall, the Tununk Shale member of the Mancos Shale is mapped (Doelling et al., 2015). This unit is underlain by the Dakota and Cedar Mountain formations, and the Bushy Basin, Salt Wash, and Tidwell Members of the Morrison Formation. Underlying the Morrison formation is the Summerville, the Curtis formation and the Entrada Sandstone. The Carmel Formation consists of shales and silts and represents the caprock to the underlying Navajo Sandstone CO2 reservoir.

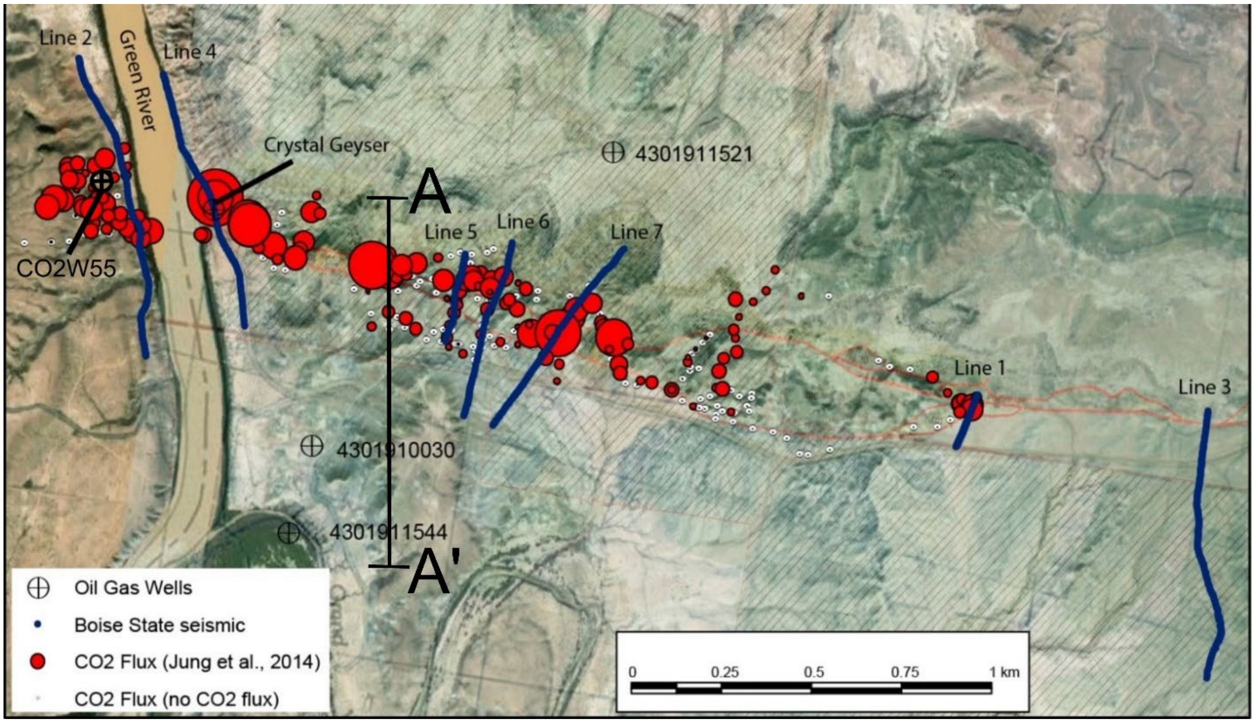

Figure 2.2 Map of the study area with collected seismic lines (blue), CO2 measurements by Jung (2014) (red circles are proportional to amount of measured flux), and locations of local boreholes identified by API number or by name. The mapped fault trace locations are indicated by the red lines and the location of cross section A-A' (Figure 2.3) is also shown.

Crystal Geyser and Travertines

The Crystal Geyser region is a prominent area for studying naturally-leaking CO2 around the world (e.g., Jung, 2014). Along the fault, CO2 driven geysers and springs appear, as well as active and ancient travertine deposits with carbonate veining. Uranium/Thorium (U/Th) dating, age dating of the ancient travertine implies the occurrence of constant CO2 leakage during the last 114,098 +/- 646 years (Burnside, 2013). Non-active travertines among active deposits indicate temporal changes in pathways for CO2 outgassing. Pathway changes can result from fracture self-sealing via carbonate vein development, earthquakes, or changes in supplying aquifer conditions.

The nearby Salt Wash Graben area (Figure 2.0) also has a series of springs and geysers. Travertine deposits along this neighboring fault system have been dated as long as 413,474 +/- 115,127 (2σ) years (Burnside, 2013).

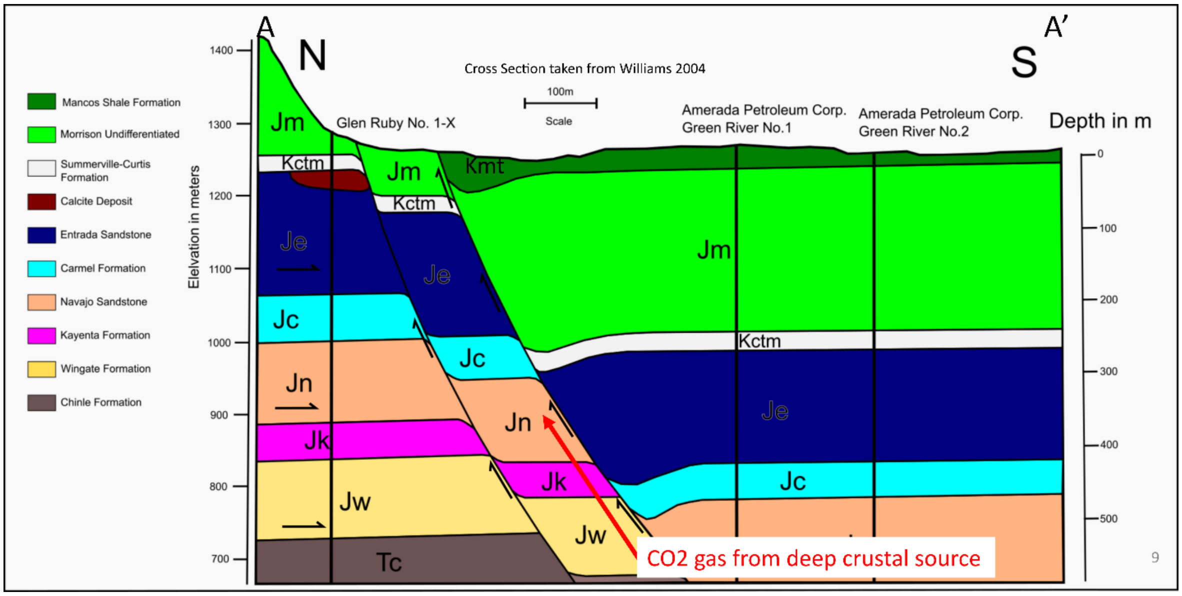

Figure 2.3 Cross section A to A' (Figure 2.2) adapted from AP Williams (2004) based on local boreholes (vertical black lines) listed along surface. Black arrows indicate fluid flow within sandstone reservoir formations and upward along the LGWF. Red arrow indicates CO2 gas flow.

Local Boreholes

Borehole data from the region help constrain interpretative cross sections (Figure 2.4). Crystal Geyser (Figure 2.2) is the result of an abandoned hydrocarbon exploratory drill-hole Ruby X-1 drilled in 1935 which reached a total depth of ~800 m in the upper portions of the Permian White Rim Sandstone (Baer and Rigby, 1978). The shallowest CO2 gas zone was observed in a calcite zone that ranged from 8.8m to 18 m depth.

The 322 m deep CO2W55 scientific borehole is located directly west of the Green River and Crystal Geyser (Kampman et al., 2014; Figure 2.2). The borehole encountered the Entrada Sandstone in the upper 150 m, the Carmel sandstones and shales from 150-

200 m, and the Navajo Sandstone from 200 to 322 m. Gas presence was intermittent through the Entrada Sandstone, not seen in the Carmel formation, and constant through the Navajo. This well was also plugged and abandoned due to abnormally high fluid pressures.

Greentown Fed 35-12, or API 430931507, was drilled and abandoned by Delta Petroleum Corporation in December, 1990 (Figure 2.2). It is located 750 m north of the LGWF, and reaches a total depth of 1066 m. The drilling log states the Entrada Sandstone was reached at 137 m depth, the Carmel at 287m and the Navajo Sandstone at a depth of 331m.

Approximately 750 m to the south of the LGWF, the 1720 m deep Amerada Green River Unit #1, API 4301910030, was drilled in 1948 and later abandoned Unit #1 (Figure 2.2). This well encountered the tops of the Entrada Sandstone, Carmel Formation, and Navajo Sandstone at depths of 263 m, 404 m, and 455 m respectively.

Roughly 1000 m east and 300 meters north of Crystal Geyser, the 1164 m deep Marland Oil #1, API430911521 borehole (Figure 2.2) encountered the top of Entrada Sandstone at 190 m depth, the Carmel at 292 m, the Navajo at 344 m, the Kayenta Formation at 457 m, and the Wingate Sandstone at 498 m.

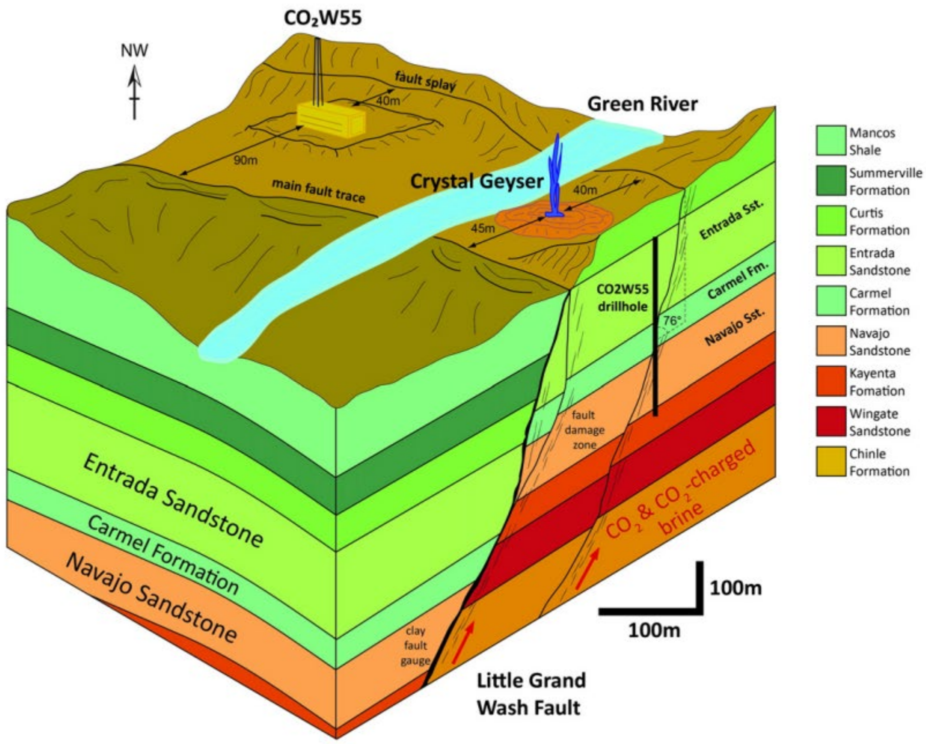

Figure 2.4 Cross section from Kampman et al. (2014) of the area near borehole CO2W55 showing the location of the Little Grand Wash fault in relation to Crystal Geyser.

CO2 Brine System

There are a number of hypotheses for the origin of CO2 in the LGWF system. Baer and Rigby (1978) interpreted the CO2 source to be chemical reactions of meteoric groundwater within the Navajo Sandstone (Figure 2.3). Shipton et al. (2004) proposed thermal decomposition of carbonate rocks in a formation at greater than 800 meters depth. Similar to the idea of Baer and Rigby, (1978), Assayag et al. (2009) hypothesized that free CO2 gas originates by exsolution from saturated Navajo brine. Analyses of in situ water chemistry sampled from drill-hole CO2W55 suggests a deeper crustal source at depths greater than two km, migrating along the LGWF as a dissolved brine to feed shallow aquifers (Jung, 2014). Based on analysis of helium and carbon isotopes in gaseous CO2 by Heath et al. (2009), CO2 may originate at a depth of over 800 m as a product of clay-carbonate reactions, thermal degradation or a combination of both processes. Wilkenson et al. (2009) collected and analyzed gas samples from Crystal Geyser as well as other nearby geysers. Based on those findings, 1-20% of CO_2 by volume originated in the mantle with the remainder derived from crustal sources (Han et al., 2013).

Dissolved CO_2 brine mixes with meteoric waters in shallow aquifers within the Navajo and Entrada Sandstone formations. Waters sampled from Crystal Geyser have been found to contain meteoric mixtures consistent with parts of the San Rafael Swell recharge area (Kampman et al., 2014). This suggests meteoric ground water recharge flows from the northwest to the southeast into the source aquifers of the Geyser (Jung, 2014). The study of scientific drill-hole CO2W55 reports free CO_2 gas in the Entrada Sandstone and only CO_2 charged fluids with no gas in the Navajo Sandstone (Kampman et al., 2014). CO_2 migrates upward into the trap created by the Green River anticline along the northern damage zone of the Little Grand Wash fault. CO_2 outgasses to the surface in seeps localized to areas in which there is fracturing and where fluid pressures reduce the effective horizontal stress to approximately zero (Naruk et al., 2019). The combination of fracturing in the fault damage zone with high fluid pressure opening fractures further increases permeability and allows the fault damage zone to be a vertical conduit for CO_2 and water. The high fluid pressure may also act to prevent diagenesis within the damage zone, a possible factor in the lengthy duration of CO_2 outgassing at the site.

CHAPTER THREE: SEISMIC DATA

Acquisition

A team from Boise State collected seismic data over the course of two field campaigns (Table 3.1). A total of eight hammer seismic surveys were acquired. Surveys were all designed to transect the fault in areas with either relatively high or minimal CO2 flux measured along profile (Figure 2.2). The most suitable terrain for geophysical surveys is found in low elevation drainages incised into the slope at the base of the cliffs. These allow survey profiles to intersect the mapped fault traces with both a near perpendicular angle and adequate subsurface coverage on each side of the fault zone (Figure 2.2). Locations for surveys east of Crystal Geyser are limited by 260-300 m tall cliffs on the footwall side of the LGWF. Here, seismic acquisition took place by hand and a sledge-hammer source. We acquired both vertically and horizontally polarized hammer data along one profile. Two profiles were acquired with the use of an accelerated weight drop source. Line 1 and Line 4 profiles were not used in my analysis.

Table 3.1 Details pertaining to each collected survey for the duration of the project.

Line #	Summary
Line 2	• Collected January 18th, 2020 • N-S transect along dirt road that spanned the western bank of the Green River. • Seismic source was a trailered accelerated weight drop (35kg), four shots per source location at midpoints between geophones • Two 120 geophone spreads at 5m spacing, overlapped for total span of 800 m • GPS locations of both source and receiver positions were collected during survey
Line 3	• Collected January 20th, 2020 • N-S transect along dirt road Crystal Geyser Safari Route. • 144 geophones at 5m spacing, 720 m total span • 4.5kg hammer and strike plate was source north of road and a 35kg accelerated weight drop.
Line 5	• Collected October 6th, 2019 • N-S transect located along a drainage approx. 800 m east of Crystal Geyser • 120 geophones at 2m spacing, total span 240m • 4.5kg sledge hammer on aluminum strike plate source locations at each half station moving north to south
Line 6	• Collected October 5th, 2019 • N-S transect along a drainage approx. 925 m east of Crystal Geyser • 96 geophones w/ 5 m spacing, 480 meters total span • 4.5kg sledge hammer on an aluminum strike plate
Line 7	• Collected October 3rd, 2019 • N-S transect along drainage gulch approx. 1 km east of Crystal Geyser • 120 vertical component geophones at 5m spacing, total span 600m • 4.5kg sledge hammer on an aluminum strike plate
Line 7 shear wave	• Collected October 3rd, 2019 • N-S transect along drainage gulch approx. 1 km east of Crystal Geyser • 96 horizontal component geophones at 5m spacing, total span 480m • 4.5 kg hammer source on aluminum plate on the side of a wooden block, 4 shots east direction and 4 shots west direction.

Line 2

The north-to-south, 800 m long seismic Line 2 is located along the western bank of the Green River (Figure 2.2). Motivation for collecting Line 2 was to compare formation depths interpreted from the W55 borehole log, the relatively flat footwall topography, no traffic, and proximity to the geyser without the affiliated ambient noise. This survey consisted of 120 recorded channels using 10 Hz vertical geophones spaced at five meters apart. A total of 168 source and geophone points were recorded, with the movement of 48 geophones to the south end of the profile during acquisition. A 35 kg accelerated weight drop was used to collect four shot gathers at each midpoint between geophones. Several shot points along this survey were inaccessible due to road washouts. I present both first arrival Vp tomography and reflection results from this profile.

The Line 2 elevation ranges from 1234 to 1243 m, with all positions less than 10 m above the Green River (Figure 2.2). Measured from the north, the profile crosses the LGWF at a distance of approximately 500 m along the profile (Doelling et al., 2015) (Figure 2.1). Kampman et al. (2014) mapped a second trace 360m from the north end of the profile. Line 2 crosses approximately 50m east of the CO2W55 borehole at the 400 m distance of the profile (Figure 2.2). To the north of the fault, rocks of the Summerville-Curtis Formation and modern river deposits are mapped. Downhole logs from regional boreholes suggest that the Summerville-Curtis unit is upwards of 50 m thick. To the south of the fault, surface geology is mapped as a thin layer of Dakota/Cedar Mountain Formation and Mancos Shale along-side terrace alluvium deposits (Doelling et al., 2015, Kampman et al., 2014). CO2 flux measurements ranged from 2.4 to 111.3 g.m^2/day from position 250 to 500 m along the profile (Jung, 2014). The highest levels recorded were near the 500 m mark of that range adjacent to travertine aged to be 5029 +/- 31 years old by Uranium/Thorium (U/Th) dating.

Line 3

Line 3 is located along the Crystal Geyser Safari Route approximately three km east of Green River (Figure 2.2). The profile consisted of 144 10 Hz vertical geophones spaced five meters apart for a total span of 720m. The northern 130 m was located to the north of Little Valley Road. Here, we used a 10 lbs. sledge hammer source. To the south, we used an accelerated weight drop along the Crystal Geyser Safari Route. The northern 10-15 m of Line 3 lies on the fault's footwall, where Bushy-Basin member of the Morrison formation is mapped. The southern hanging wall side of the LGWF is mapped by Doelling et al. (2015) as Mancos Shale. The north end of Line 3 includes steep elevation along a cliff base. To the south, mostly flat terrain was encountered. No measurements of CO2 flux were made along this profile (Jung, 2014; Figure 2.2). I present both first arrival Vp tomography and reflection results from this profile.

Line 5

Line 5 is located along a drainage approximately 700 m east of Crystal Geyser (Figure 2.2). The survey consisted of 120 10-Hz vertical geophones placed at two-meter spacing totaling a profile span of 240 m. The source for each shot gather was a 10 lbs. sledge hammer struck on an aluminum plate. Four shot gathers were collected at each shot point located at the midpoints between geophones. The elevation of Line 5 lies 30-50 m above the elevation of the Green River. Line 5 is the highest elevation seismic profile with an elevation range of 1257 m to 1293 m. In a previous study, CO2 flux values of 0.7 to 11.2 g/m^2/day were measured along the Line 5 transect (Jung, 2014;

Figure 2.2). Surface geology of Line 5 is mapped as Summerville formation sandstone on the footwall side, Mancos Shale on the hanging wall side and Bushy-Basin member of the Morrison formation within the span between fault traces (Doelling et al., 2015). I present first arrival Vp tomography results from this profile.

Line 6

Line 6 is located along a drainage approximately 880 m east of Crystal Geyser (Figure 2.1). The survey consists of 96 10 Hz vertical geophones spaced 5 meters apart for a total profile span of 480m. The source for each shot gather was a 10 lbs. sledge hammer against an aluminum strike plate. Four shot gathers were collected at each shot point located at the midpoints between geophones. Elevations at 30-40 m above the Green River suggest a deeper water table compared to the other profiles. To the north, Doelling et al. (2015) mapped sandstone rocks of the Summerville Formation. Downhole logs from regional boreholes suggest that the Summerville unit is upwards of 50 m thick. This unit overlies the Curtis Formation and Entrada Sandstone Formation. Between the northern and southern fault traces, the Bushy Basin Member of the Morrison Formation is mapped. To the south of the fault, Doelling et al. (2015) mapped rocks of the Tununk Member of the Mancos Shale Formation. This unit is estimated to be less than 24 m thick from local borehole Amerada Green River Unit-#1 and lies above the fluvial sandstone Dakota formation and siltstone/mudstone rich Cedar Mountain Formations. CO2 flux measurements along Line 6 range from 1.7 to 38.7 g/m^2/day (Jung, 2014). I present first arrival Vp tomography results from this profile.

Line 7

Line 7 is a 600-meter-long survey centered roughly one km east of Crystal Geyser (Figure 2.1). The profile runs along a drainage that cuts further into the north bordering cliff slope compared to Lines 5 and 6. This allowed for a greater total profile length, enabling longer source-receiver offsets and deeper probing depths when compared to Lines 5 and 6. On the northern footwall block, Doelling et al. (2015) mapped sandstone rocks of the Summerville Formation to a depth of about 50 m. The Summerville Formation lies above the high porosity Entrada Sandstone that stores CO2. In the hanging wall block to the south of the fault, Doelling et al. (2015) mapped Quaternary alluvial deposits overlying rocks of the Mancos Shale formation. Line 7 transects the fault at an NE-SW trend due to the drainage orientation and intersects relatively high CO2 flux measurements, ranging from 16.7 to 5517.4 g/m^2/day. Peak CO2 was measured near where fault traces are mapped (Jung, 2014).

This Vp survey consisted of 120 recorded channels using 10 Hz vertical geophones spaced at five meters apart. I also acquired a shear wave dataset along Line 7 (Figure 2.1). For this survey, 96 horizontal component 10 Hz geophones were collocated with their vertical component counterparts starting from the north end. The shear wave survey had a total span of 480 m, A 10 lb. sledge hammer is the source for the line 7 shear wave survey. Aluminum strike plate was mounted on the sides of a wooden block to reorient the source motion to horizontal. At each shot location 4 shot gathers were collected with source motion initiating eastward, then 4 shot gathers were collected with source motion initiated westward at the same shot location.

First Arrival Tomography

I pre-processed the seismic data by assigning source-receiver geometries from differentially corrected GPS positions, removing bad traces, and bandpass filtering. I stacked common source-receiver traces to improve signal quality. I picked coherent first motions that contained a center frequency of about 50 Hz. I follow the approach of St. Clair (2015) to obtain final tomographic velocity models from my first arrival picks. I start with a 10-layer one-dimensional velocity model that incorporates topography. I then calculated the difference between my picks and calculated arrival times derived from ray tracing. I iterate from the initial model to generate two-dimensional velocity models that minimize the root mean square (RMS) model misfit. This code replaces the starting model with each iteration.

I used the inversion code of St. Clair (2015) to generate final tomograms. I modified this approach to include sparse regularization constraints using the shortest path ray tracing method of Moser (1991). Sparse regularization constraints seek to minimize the L1 norm on model smoothness by allowing sharp boundaries to appear in the solution. The objective function is

$$\varphi = min\{||Am - d||_2^2 + \alpha_x |L_x m|_1 + \alpha_z |L_z m|_1\} \qquad (7)$$

where A is the Fréchet matrix, m is the model vector, d is the data vector, L_i are derivative operators and α_i are regularization weights. Thus, we minimize the L2 norm of the data misfit, but the L1 norm of the model smoothness constraint.

I employed an iterative reweighting algorithm to solve the problem. First, I solve:

$$dm^j = [A^T A + \alpha_x^2 L_x^T L_x + \alpha_z^2 L_z^T L_z]^{-1}[A^T d - [\alpha_x^2 L_x^T L_x + \alpha_z^2 L_z^T L_z]m^j] \qquad (8)$$

where dm^j is an update vector for the current model vector m^j. Next, I apply the derivative operators to the new model $m^{j+1} = m^j + dm^j$ to get the magnitude of $\alpha_i L_i m^{j+1}$ at every model parameter. Then, I solve the new problem:

$$dm^{j+1} = [A^T A + \alpha_x^2 L_x^T W_x L_x + \alpha_z^2 L_z^T W_z L_z]^{-1}[A^T d - [\alpha_x^2 L_x^T W_x L_x + \alpha_z^2 L_z^T W_z L_z]m^{j+1}] \qquad (9)$$

where

$$W_i = diag[\left(L_i m^{j+1} + \epsilon\right)^{-1}] \qquad (10)$$

for $\epsilon \ll 1$. We repeat this process until $1^T\left(\alpha_x L_x m^{j+1} + \alpha_z L_z m^{j+1}\right) - 1^T\left(\alpha_x L_x m^j + \alpha_z L_z m^j\right) < \tau$, for some predefined τ (St. Clair, 2015). Metric of model fit τ is the calculated difference of observed versus calculated arrival times, or root mean square (rms) error.

The code utilizes Tikhonov regularization, a method of regularization for ill-posed problems with no unique solution. There is a regularization parameter to weight the velocity gradient linearly with depth and I have 1st and 2nd derivative parameters that constrain both vertical and horizontal smoothness of the model. Reweighting parameters can help smooth anomalous model features but generally can remove larger primary features in the model. Regularization parameters can be updated in each iteration to improve model fit. Through ray tracing, I determine that velocity models are well constrained for the upper 20 to 40 meters below land surface. For a final model, I iterate until I obtain a misfit, or sum of all RMS values, less than .005 s or until RMS values change by less than .001 s from the previous iteration. To validate that model, I compare final tomograms to first break picks on shot gathers that cross the fault to ensure that velocity reduction corresponds to the regions in which velocity structures exist (Figure 3.0).

The Common Offset Gather

I adopt the use of common offset gathers (COG) to identify lateral seismic boundaries and to validate my final tomographic models (Figure 3.0). This approach has been used to map faults and to validate large lateral velocity changes (e.g., Schuster et al., 2016; Liberty et al., 2021). With this approach, I assume that first arrival travel times and surface wave phase velocities will remain constant for a fixed source/receiver offset. Visible and large changes in these arrivals suggest the presence of a lateral boundary. For example, Figure 3.0 shows slower first arrivals near positions 2075 and 2100 along the deconvolved Line 2 COG. Deconvolution attenuates wave path multiples and sharpens the seismic pulse (Yilmaz, 2001). These surface locations coincide with the mapped fault trace of Doelling et al. (2015). The low passband COG also shows changing wave speeds for the surface waves to the south of the mapped fault trace. By removing higher frequencies from the COG, surface wave signals are highlighted.

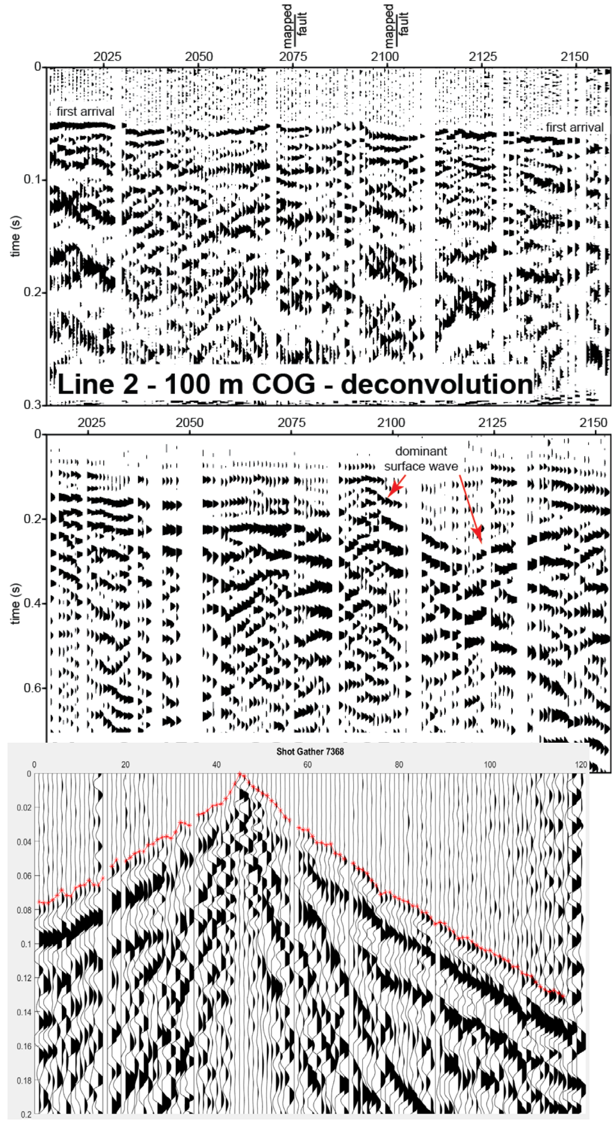

Figure 3.0 Shot Gather (top) from line 7 showing first arrival picks (red) with distance along profile in the x direction and time in seconds in the y direction. In the center is a common offset gather with an applied low-pass filter. The bottom image is a 100m depth common offset gather deconvolution.

Tomographic Results

Line 2

My final tomogram for Line 2 shows an RMS error of .0027 s with ray coverage to about 30 m depth. Vp ranges from 500 to 3500 m/s. I observe a vertical velocity gradient that ranges from 50 to 60 m/s/m. The depth to the 1500 m/s contour is close to the measured Green River surface elevation of 1228.5 m. The river elevation and Vp values suggest water saturated sediments are found at a depth of a few meters. The depth to the 2000 m/s contour ranges from 2 to 15 m depth. From the W055 borehole, located about 70 m to the west of position 400 m (Figure 2.2), Kampman et al. (2014) identified the regolith base at 10.2 m depth, consistent with this velocity contour. Below, they identified the gas-rich Entrada sandstone to 149 m depth.

At 500 m distance, I observe a 30 m wide slow, low gradient Vp zone at all measured depths. I interpret this Vp reduction as the fault damage zone, as it corresponds with a previous mapped fault strand (Kampman et al., 2014) (Figure 2.2). The resulting low Vp implies an increased ϕ (Figure 3.1) (Castagna et al., 1985; Caine et al., 1996) where I speculate that high fluid and gas pressure has widened pre-existing microfractures (Naruk et al., 2019). Elevated CO2 flux values were measured between 270 to 520 m distance along Line 2 (Jung, 2014), and I observed gas bubbles surfacing along the bank of the Green River near position 500 m. Both of these observations suggest that the high porosity damage zone represents a high permeability conduit for upward flowing CO2. Although elevated CO2 was observed near the northern fault trace at position 350 m, I observe no measurable Vp change in the upper 10 m. However, I observe lower Vp and likely higher ϕ north to about 350 m distance below the regolith base, as defined by Vp=2000 m/s contour. This may imply some diffusive CO2 flow through the unsaturated regolith, consistent with observations of Jung, (2014). Near the lower boundary of my model, between 100 m to 350 m distance, I estimate ϕ <0.25 that is consistent with unaltered Entrada sandstones. To the south of the fault, Vp is generally less than that observed to the north of the fault. This observation is consistent with mapped shales (Doelling et al., 2015). At position 690m distance, I identify a slow Vp zone that does not correspond with a mapped fault. I speculate this may be a minor fault or fracture zone. There are no measured CO2 flux values at this position.

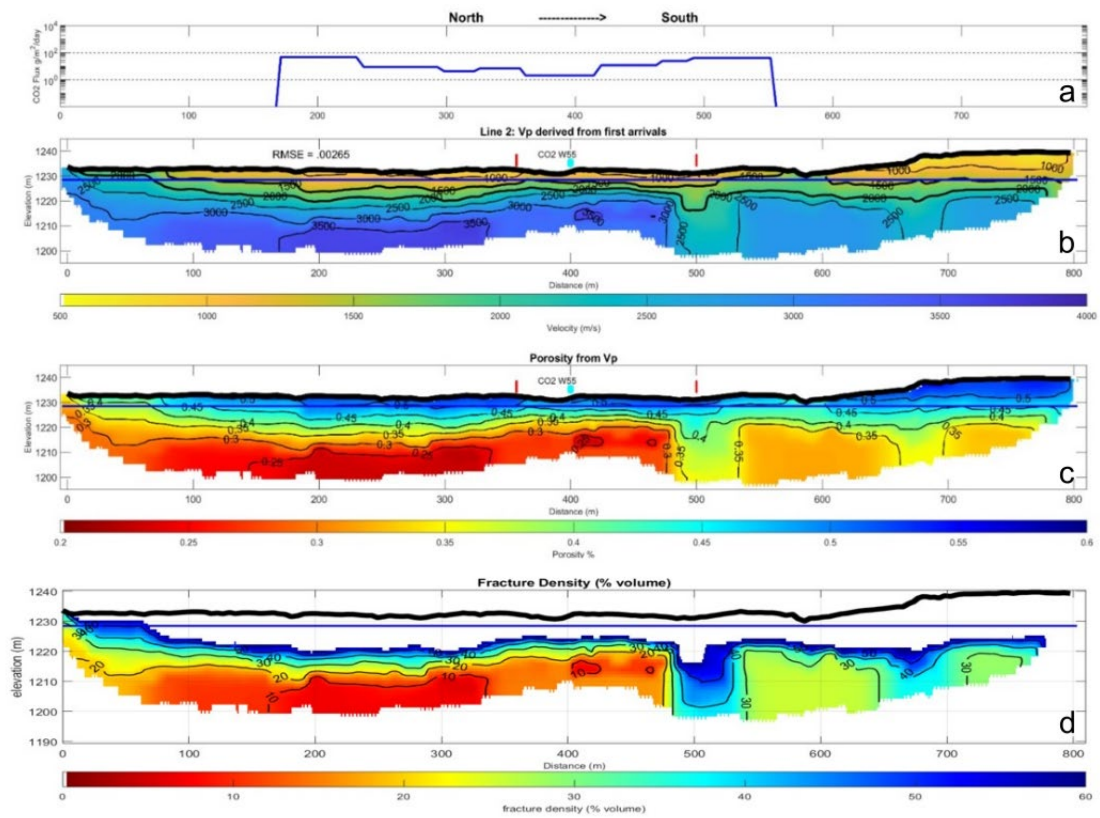

Figure 3.1 Line 2 CO2 flux measurements of Jung (2014) (a) and refraction tomogram model at 2:1 vertical exaggeration (b) showing mapped locations of two LGWF strands. Porosity estimates the relationships of Castagna et al. (1985) (Figure 1.1, equation 1) (c). Red lines are mapped fault locations (E. Petrie, personal comm.). Estimated fracture density (d) from Clark and Burbank (2011).

From simple rock physics relationships (Figure 1.1), I interpret unsaturated and saturated unconsolidated sediment and unsaturated and saturated consolidated rock for Line 2 (Figure 3.3). I interpret unsaturated soils and regolith above the water table or river elevation. These soils measure Vp<1500 m/s. Below, I interpret saturated regolith that extends from 10 to 30 m depth or Vp between 1500 to 2500 m/s. Semi-consolidated bedrock lies below the regolith and refers to heavily fractured bedrock to semi-consolidated soils that were identified in borehole W055. This unit Vp ranges from 2500 to 3000 m/s. I term consolidated bedrock for materials that have much lower fracture density but where minor fracturing is still present. Vp ranges from 3000 to 3500 m/s. Finally, unaltered bedrock represents unfractured, un-weathered host rock where Vp>3500 m/s. This velocity is consistent with a sandstone of 20% porosity and 20% clay (Equation 1).

For my geologic interpretation (Figure 3.2), the slow velocity zones at position 500 m and 690 m appear as saturated regolith within the damage zones of faults of the LGWF. Although not mapped, I interpret this second fault strand at 690 m, A change from consolidated bedrock to semi-consolidated can be seen across the interpreted fault damage zone, this is likely a change in lithology from Summerville formation in the north to Cedar Mountain formation to the south as mapped by Doelling et al. (2015).

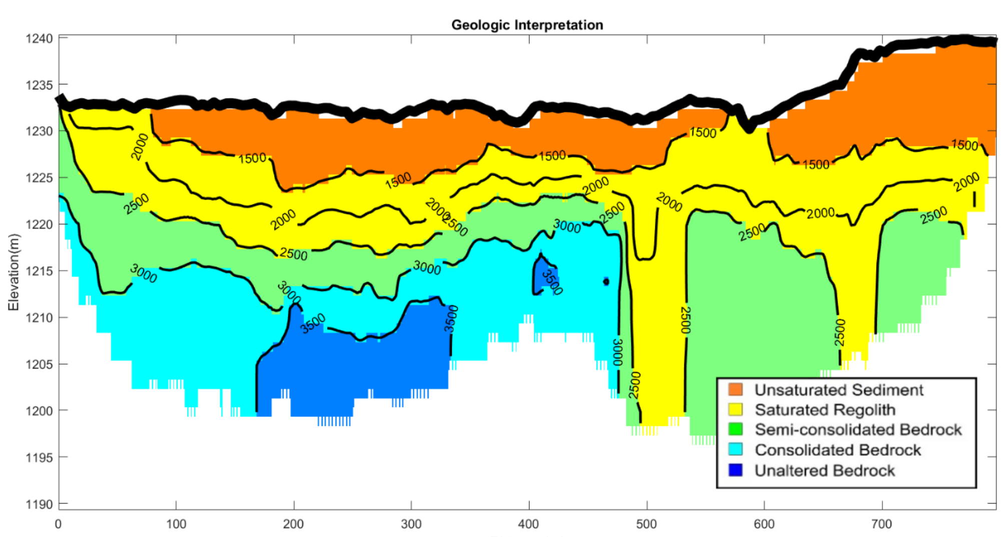

Figure 3.2 Geologic interpretation based on values from Lee (2003) (Figure 1.1).

Line 3

The 600 m long Line 3 tomogram (Figure 3.3) is located three km to the east of the Crystal Geyser, and crosses the LGWF approximately 10-15 m from the north end of the profile (Figure 2.1). My final velocity model, with an RMS error of .00154 s, shows Vp that ranges from 1500 to 3500 m/s. I observe a vertical velocity gradient that ranges from 50 to 60 m/s/m. Previous mapping of the fault location is near the northern end of the profile and may not be reliably imaged. I observe no areas of slow Vp or changing porosity estimates further south that could suggest faulting. My interpretation aligns with fault mapping of Doelling et al. (2015). From position 450 m to 550 m, I observe that Vp in the top 10 m increases from less than 2000 m/s to above 3000 m/s.

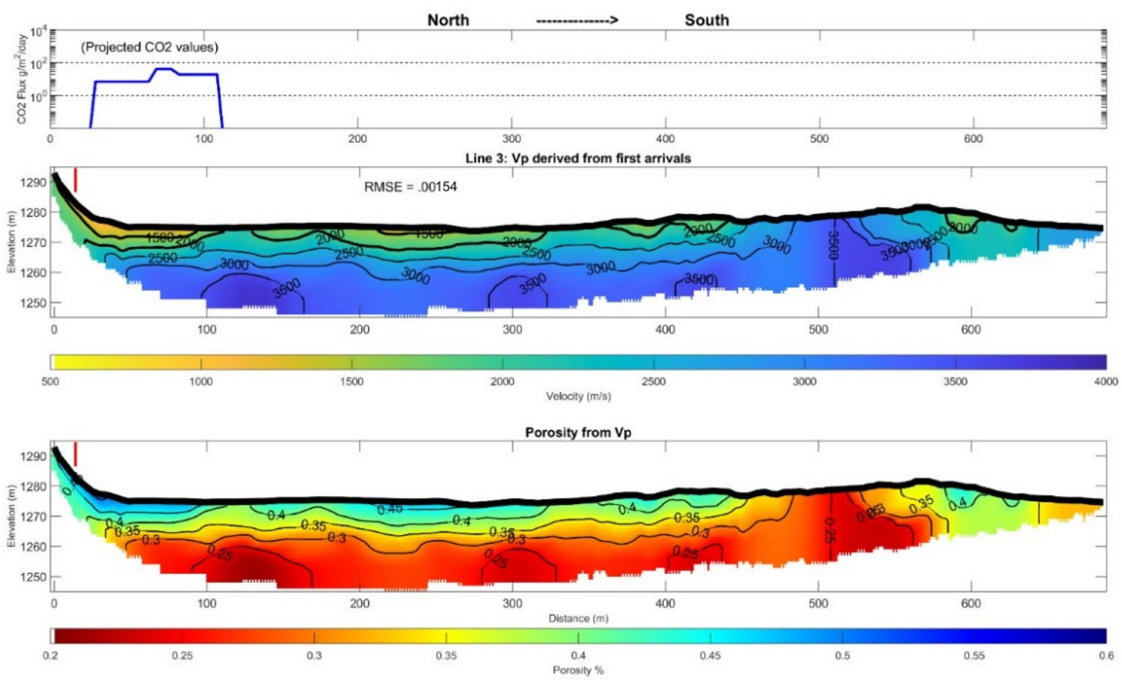

Figure 3.3 Line 3 projected CO2 flux (Jung, 2014) (top) and final refraction tomogram model at 2:1 vertical exaggeration (center). Porosity estimates the relationships of Castagna et al. (1985) (Figure 1.1, equation 1) (bottom). Red lines are mapped fault locations (E. Petrie, personal comm.).

Applying the same velocity ranges for unsaturated and saturated, unconsolidated and consolidated materials as with Line 2, I create a geologic interpretation for Line 3 (Figure 3.4). The Vp/lithology relationships for Line 3 are different when compared to the other profiles, as the mapped lithology is mostly a more clay-rich shale. Velocity/lithology relationships of Lee (2003) were from sandstones samples with lower clay content. As I show with equation 1, a greater clay content will lower the Vp with respect to porosity and can lower the Vp for consolidated rock. Regardless, from position 0 to 480 m distance, the bedrock generally lies 10 to 15 meters below ground level. I interpret saturated sediments to the near surface, as Vp is generally >1500 m/s. From position 480 to 520 meters I observe an increased velocity in the near surface. Near this position Doelling et al. (2015) mapped the crest of an anticline, the velocity increase may be the exposed compressed crest of this anticline. One other hypothesis for this high velocity zone is a fault zone that is imaged at greater depth in the Line 3 reflection image (Figure 3.14). Higher velocities would support a low permeability fault here.

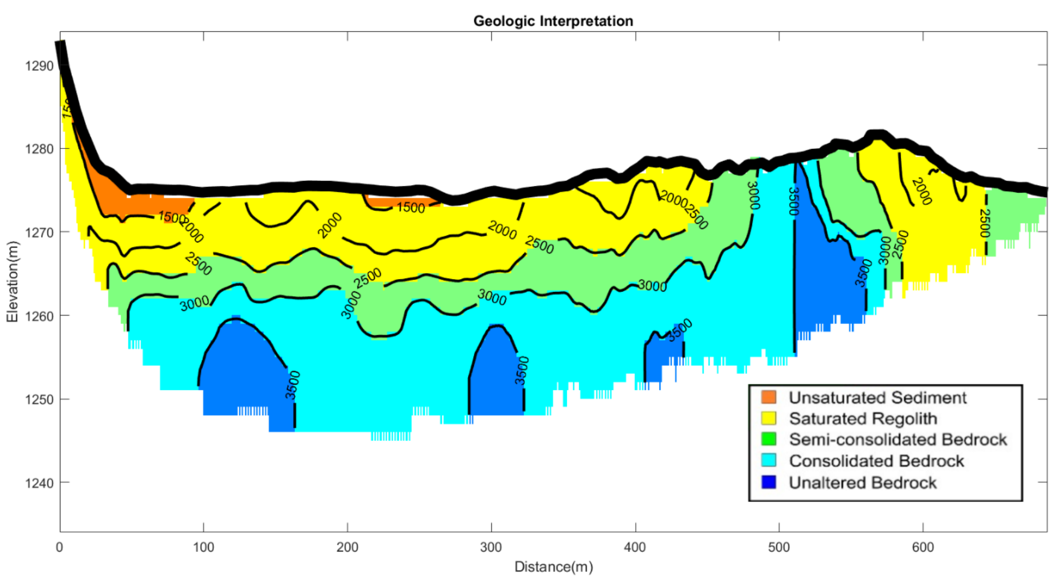

Figure 3.4 Geologic interpretation of Line 3 using velocities from Lee (2003).

Line 5

For Line 5, my final Vp model, with an RMS error of .002 s, shows a Vp range from 1000 to 3000 m/s (Figure 3.5). I observe a vertical velocity gradient that ranges from 50 to 100 m/s/m. Two strands of the LGWF were mapped at positions 70 and 125 m. At position 135 m I observe a velocity increase in the top 20 m from 1500 m/s to 2500 m/s. I observe the velocity gradient north of position 160 m to be of the lower end of the observed gradient range. The velocity gradient south of position 160 m is less gradual at around 100 m/s/m. I interpret 0 to 23 m of regolith along this profile. The relatively low Vp suggests that consolidated bedrock lies at depths below my ray coverage.

I interpret the increased Vp/decreased ϕ around position 135 m to be a fault zone and relic flow pathway that is now sealed. I speculate that the higher Vp could be result from mineral precipitation and diagenesis, or effective stress closing pre-existing fractures within the fault damage zone (Naruk et al., 2019).

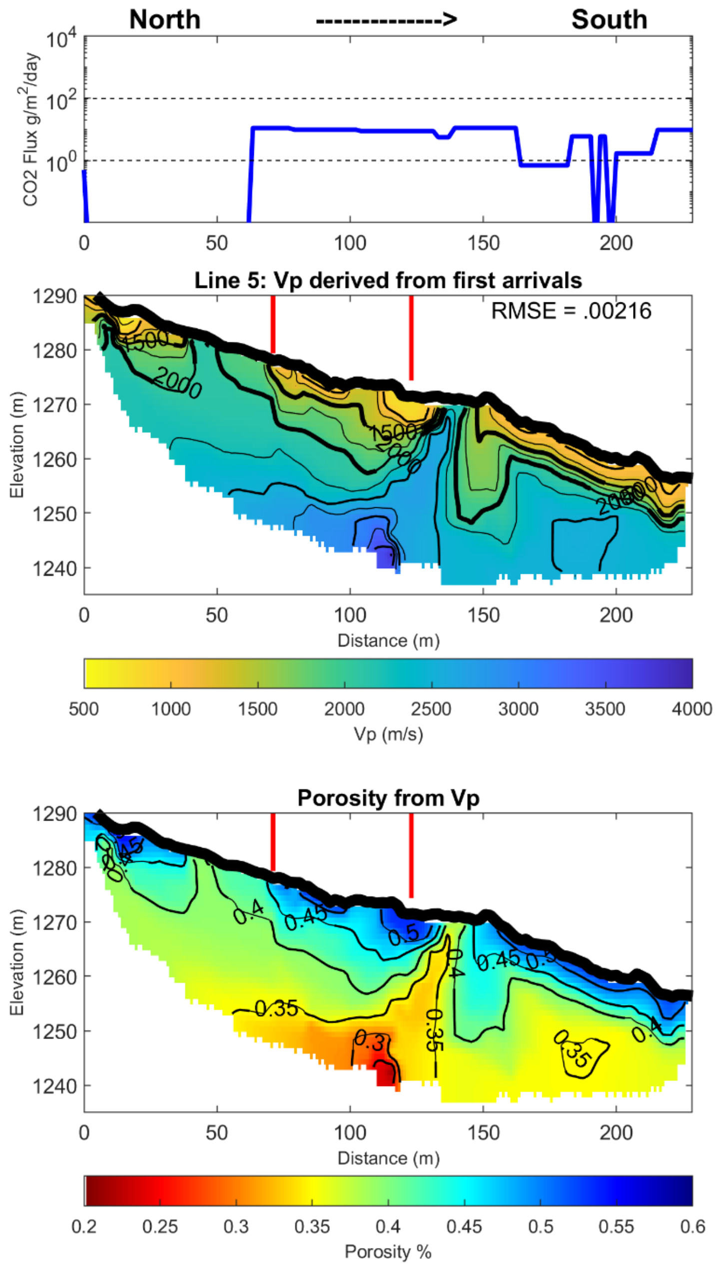

Figure 3.5 Line 5 CO2 flux profile (Jung, 2014) (top) and final refraction tomogram model at 2:1 vertical exaggeration (center). Porosity estimates the relationships of Castagna et al. (1985) (Figure 1.1, equation 1) (bottom). Red lines are mapped fault locations (E. Petrie, personal comm.).

When I apply my lithologic interpretation from Line 2, this would suggest that much of the subsurface beneath Line 5 would be represented by saturated regolith (Figure

3.6). However, Vp for saturated unconsolidated regolith at 0 MPa typically ranges from 1500 to 1800 m/s and Vp for unsaturated consolidated bedrock at 0 MPa ranges from 2000 to 2400 m/s. Both lie in the Vp range that I identify. Given the higher profile elevation with respect to groundwater levels, I prefer an interpretation of mostly unsaturated, semi-consolidated bedrock beneath Line 5.

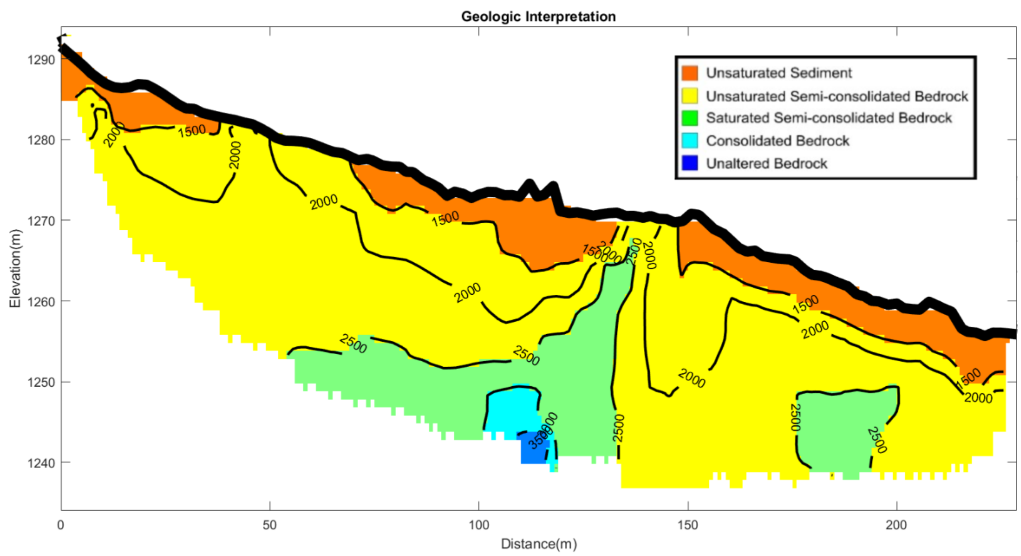

Figure 3.6 Geologic interpretation of Line 5 using Vp/lithology relationships of Lee (2003).

<u>Line 6</u>

The 480 m long Line 6 profile is located 800 m east of the Crystal Geyser, and crosses two mapped fault traces of the LGWF at a distance of approximately 135 m and 210 m (Kampman et al. 2014; Figure 2.2). My final velocity model (Figure 3.7), with an RMS error of .003 s, shows Vp ranges from 1000 to 3500 m/s. I observe a vertical velocity gradient that ranges from 40 to 60 m/s/m. Near position 210 m, I observe a slower Vp zone. This zone coincides with a mapped fault trace (E.Petrie, personal comm.). I observe a second slow Vp zone near position 300 m and speculate this may represent an unmapped fault strand. A similar slow zone is also observed at position 75

m. I speculate this may be another fault that does not correspond to the mapped traces. Measured velocities suggest 1 to 15 m of regolith, with porosities consistent with unaltered Entrada sandstone below 20 m depth. This is in contrast to the thicker regolith observed along Line 5, located 120 m to the west.

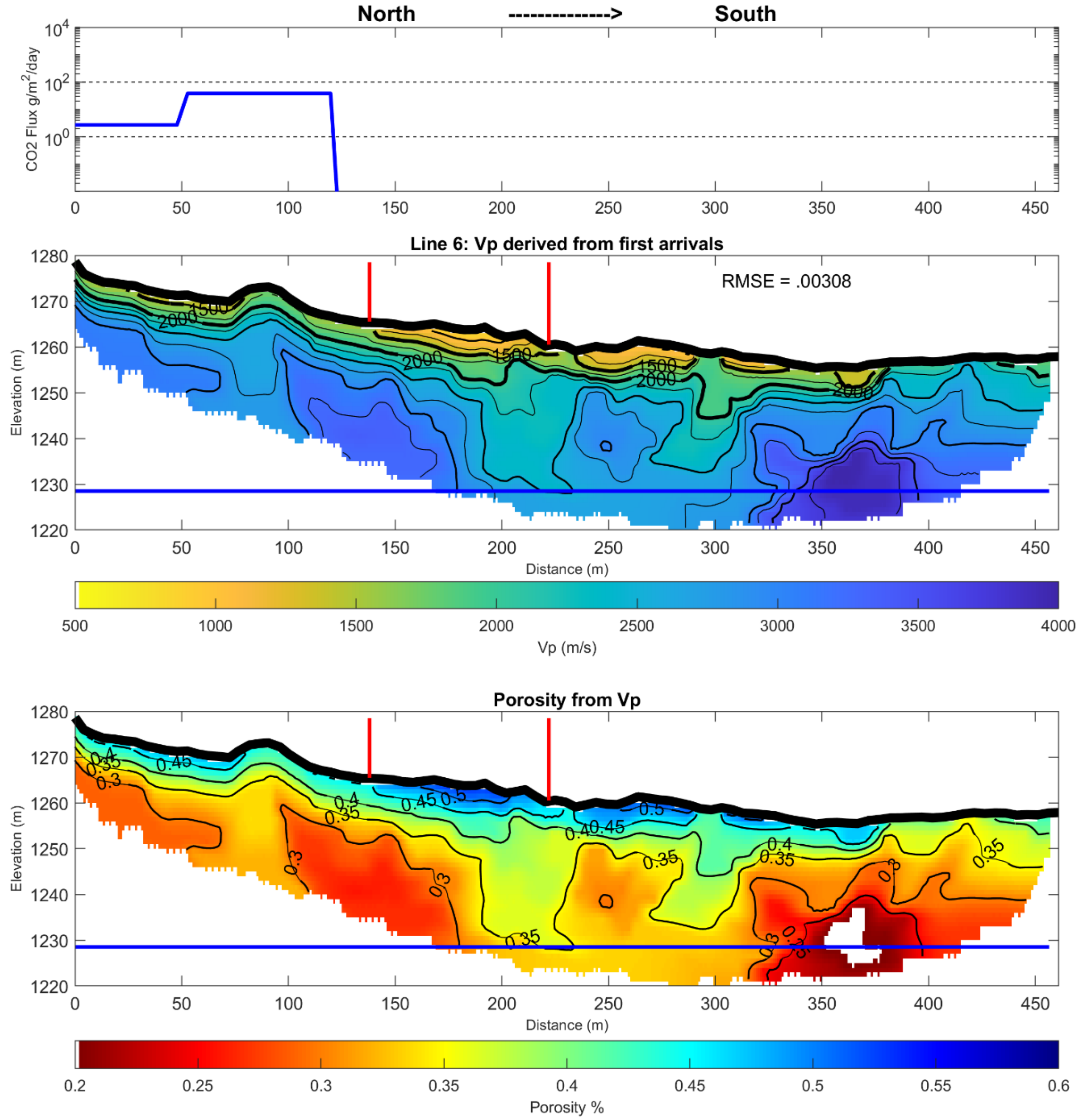

Figure 3.7 Line 6 CO2 flux profile (Jung, 2014) (top) and refraction tomogram model at 4:1 vertical exaggeration (center). Porosity estimates the relationships of Castagna et al. (1985) (Figure 1.1, equation 1) (bottom). Red lines are mapped fault locations (E. Petrie, personal comm.).

Utilizing the same Vp/lithology approach, I create a geologic interpretation for Line 6 (Figure 3.8). I categorize slow zones in my tomogram (figure 3.7) as saturated regolith or semi-consolidated material. I interpret the slow zone at position 200 m to be the southern fault trace and the zone of saturated regolith to indicate a region of highly fractured damage zone. I speculate that the slow zones at position 75 and 300 m indicate unmapped faults and that position 75 has a lower fracture density within the damage zone than position 300 m.

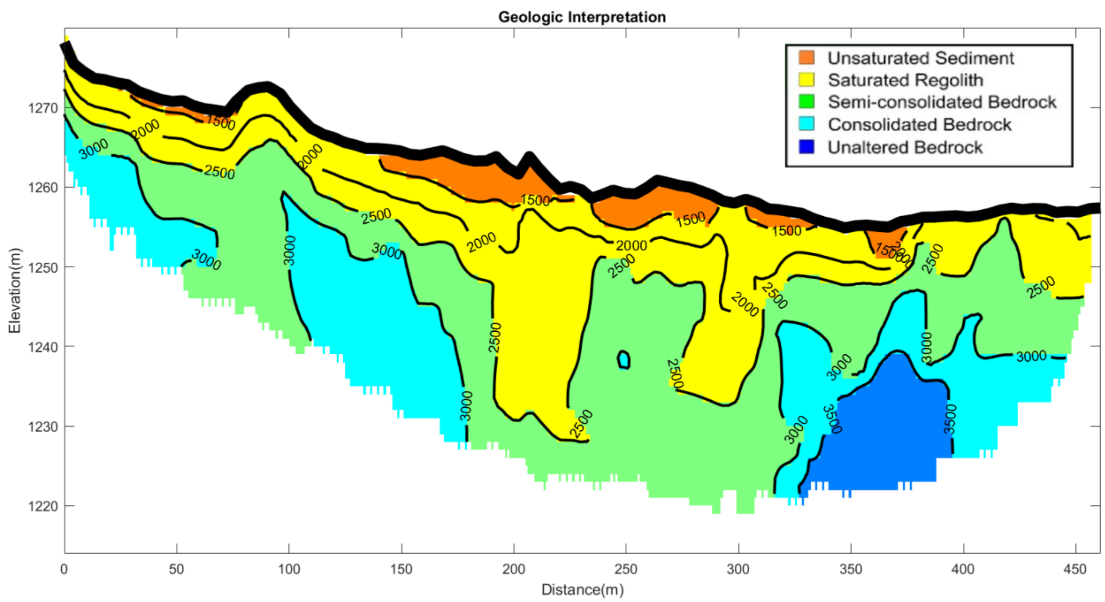

Figure 3.8 Geologic interpretation of Line 6 based on Vp/lithology relationships adapted from Lee (2003).

Line 7

The 600 m long Line 7 refraction tomogram is located 1000 m to the east of the Crystal Geyser (Figure 2.1). The dataset consists of 480 120 channel shots acquired with a sledge hammer source (four shots per source location). The profile elevation ranges from 1251 to 1267 m, between 18 to 34 m above the Green River elevation near the Crystal Geyser. The profile crosses two closely spaced 70-80 degree south dipping fault strands of the LGWF at a distance of 300 m to 340 m along the profile (E.Petrie, personal comm.). Near the southern fault location, Jung et al. (2014) mapped an area where elevated CO_2 flux was measured at 5514.7 g/m^2/day (Figure 2.2), the highest natural CO_2 source for the region. At position 250 m outgassing of water and gas bubbles flow form a natural spring. Dockrill et al. (2010) and Jung et al. (2014) suggest that the fault damage zone may range from .2 to 3 m wide. Line 7 was the only profile where I assess both Vp and Vs tomograms.

Line 7 Vp model

My final Vp model (Figure 3.9b), with an RMS error of .0026 s, shows a Vp range from 1500 to 3750 m/s. I observe a Vp increase with depth and vertical velocity gradient that ranges from 50 to 60 m/s/m. Between 300 to 340 m distance, I observe a 50 m wide zone where slower velocities are measured at all depths. In this zone velocities measure between 2000 to 2500 m/s. I interpret this zone of slower Vp to be the fault damage zone related to the southern mapped fault strand. This damge zone width is significantly greater than that mapped from surface geology. Measured velocities suggest 0 to 8 m of regolith, with porosities consistent with unaltered Entrada sandstone below 15-25 m depth. I speculate the increase in estimated porosity I observe coinciding with this slow Vp zone to suggest the fault is a pathway for fluid and gas to the surface. I further speculate that the cause of this porosity increase may be fluid pressure opening pre-existing fractures within the fault damage zone. Whereas elevated CO_2 appears across the northern fault strand, I do not observe a measurable Vp slow zone here. Instead, a faster Vp zone is observed near position 250 m. This result may suggest a relic cemented northern fault with diffusive flow through the dry regolith.

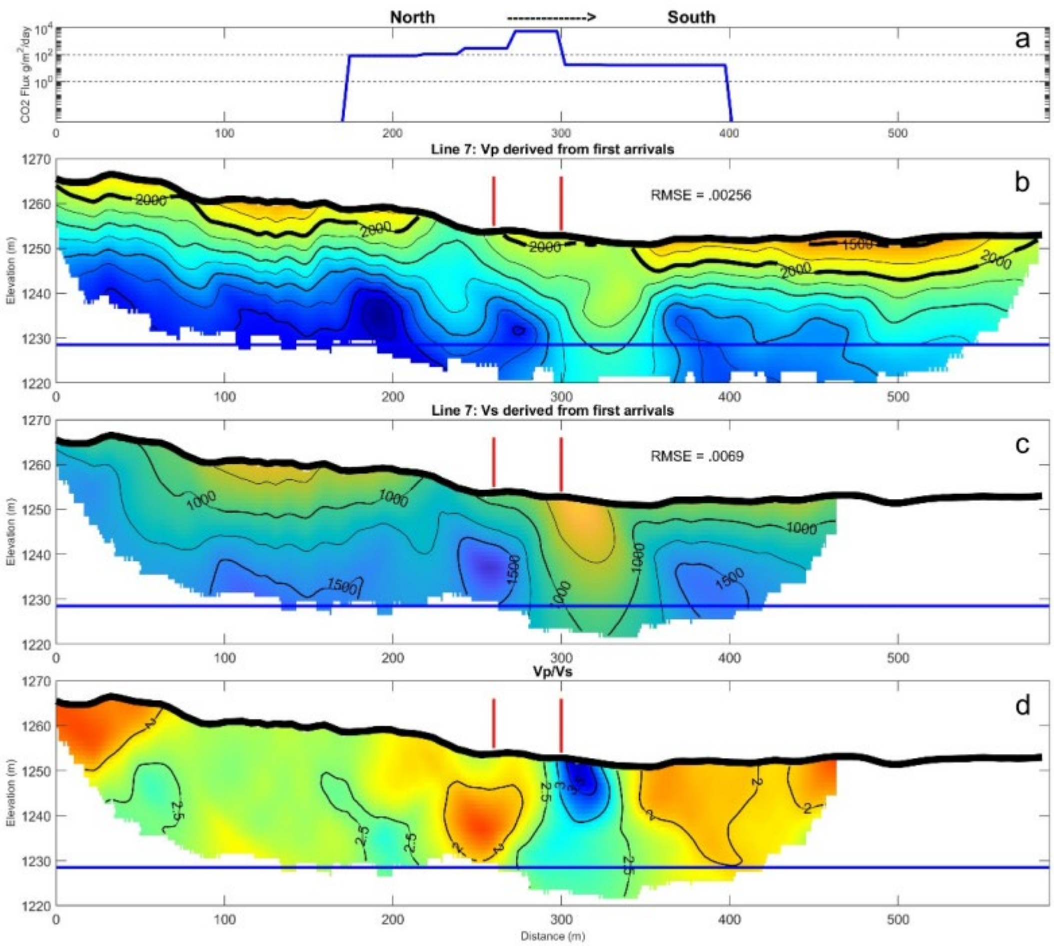

Figure 3.9 Line 7 CO2 flux profile (a) and final Vp refraction tomogram (b) model at 2:1 vertical exaggeration. Line 7 final shear wave refraction tomogram (c) model at 2:1 vertical exaggeration. Vp/Vs ratio plot (d). Red lines mark mapped fault locations (E. Petrie, personal comm.).

<u>Line 7 Vs model</u>

My final velocity model (Figure 3.9c), with an RMS error of .0069 s, shows Vs that ranges from 500 to 1750 m/s. I observe a vertical velocity gradient that ranges from 25 to 50 m/s/m. Velocities below northern portions of the profile show velocities ranging from 500 to 1800 m/s. Between 300 to 340 m distance, I observe a zone of slower velocities at all depths. These velocities range between 500 to 1000 m/s. I interpret this slow zone to be the fault damage zone. I speculate that increased porosity at this position (Figure 3.10a-c) is resultant of high pore pressure and may indicate the fault is a pathway for fluid at gas flow to the surface. Again, I see no evidence for a low Vs fault below the mapped northern fault strand.

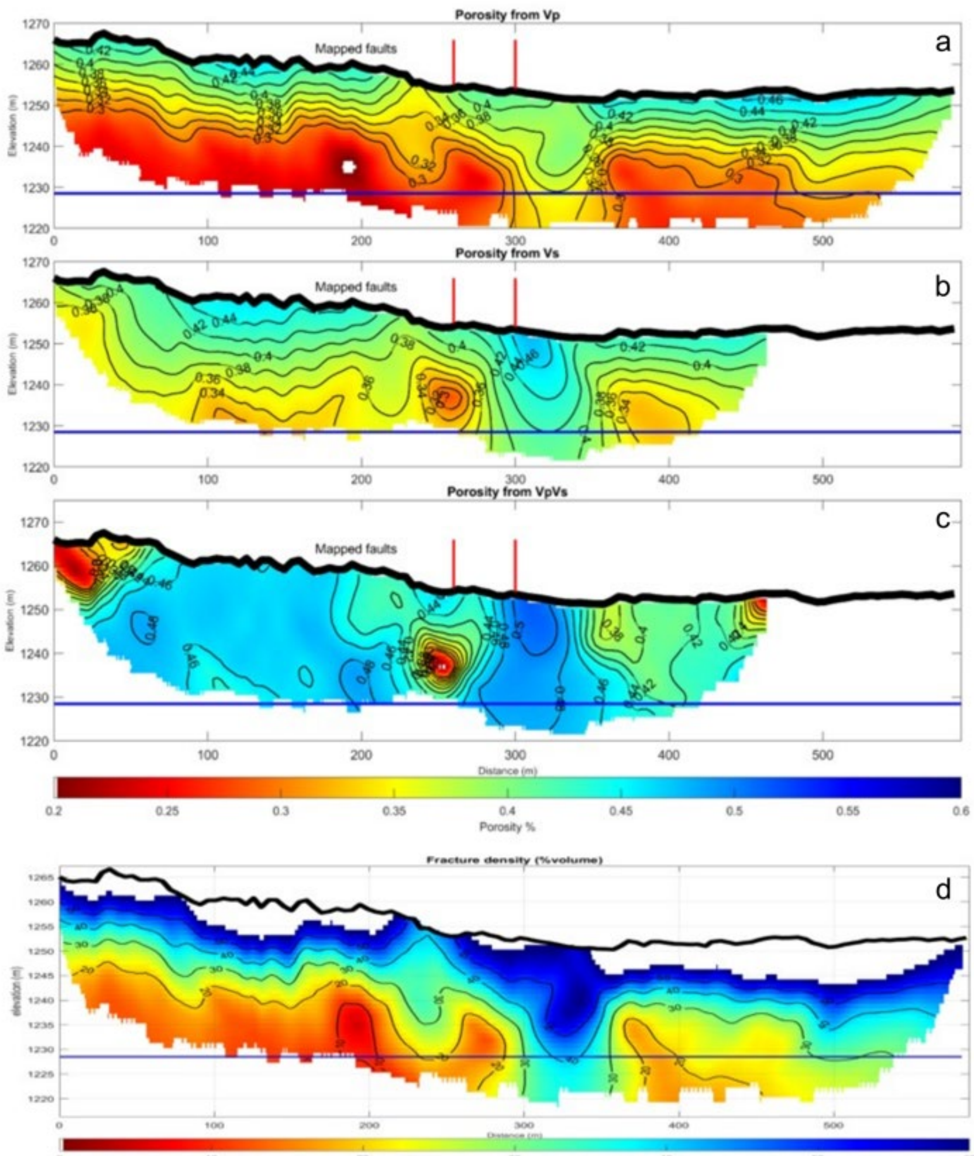

Figure 3.10 Porosity estimates of Line 7 Vp (a), shear wave (b) and Vp/Vs ratio (c) based on the relationships of Castagna et al. (1985) (Figure 1.1, equation 1-3). Estimated fracture density (d) using method from Clark and Burbank (2011).

<u>Line 7 interpretation</u>

The slow Vp and Vs zones at position 300 to 340 m correspond with a mapped fault trace of the LGWF (Figure 2.2) (Figure 3.9b-c) (E. Petrie, personal comm.). I interpret the soil/regolith and underlying rock to be saturated as Vp within the fault damage zone does not fall below 1500 m/s. The width of the damage zone observed with my seismic measurements is likely wider than that mapped with surface geology because of the lower elevations of the seismic measurements, where fluid interactions with the surface has widened the fault's damage zone.

I observe outgassing in the form of CO2 within a natural spring at position 260 m. Naruk et al. (2019) states that pore pressure can act to preserve porosity in the fault damage zone, open microfractures, and offset effective stress acting on the fault. I speculate that pressure from fluid and CO2 within pore and fracture space may cause an increase in porosity and reduce Vp within the fault zone.

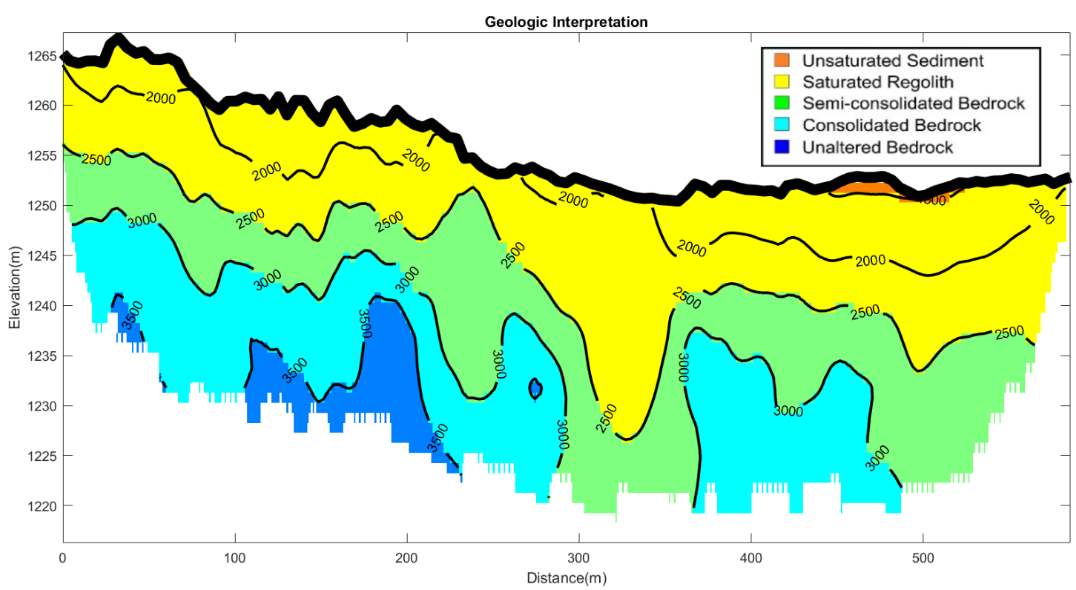

Figure 3.11 Geologic Interpretation of line 7 based on velocities from Lee (2003).

Vp/Vs Ratio

Vp/Vs is considered as a primary constraint on the nature and composition of rocks when interpreting seismological data. It is well established that the presence of fluid-filled porosity (cracks, pores or open grain junctions) strongly modifies the Vp/Vs ratio (Brantut et al. 2018). I compute the Vp/Vs ratio for Line 7 (Figure 3.9) as an estimate of fluid saturation within the profile. Since Vs is relatively insensitive to saturation, using the ratio of Vp to Vs can estimate saturation distribution more accurately than Vp or Vs alone. I interpret a Vp/Vs ratio above 2.5 as being saturated. I observe the highest Vp/Vs ratio (Figure 3.9d) to coincide with the low velocity zones in the Vp and Vs plots (Figures 3.9b and 3.9c).

Seismic Reflection

I processed three seismic reflection profiles using Halliburton's SeisSpace® processing software with a standard processing approach outlined by Yilmaz (2001). Processing steps included datum statics, spiking deconvolution, bandpass filter, surface wave attenuation through a two-step singular value decomposition approach to estimate and adaptively subtract the ground roll signal (where appropriate), iterative velocity analyses with dip moveout corrections, amplitude gains, and a post-stack time to depth conversion. Where surface waves were strong, I muted this window. Post-stack migration is selectively applied to the data where appropriate so as to not introduce migration artifacts which can distort key reflector geometries. Depths were estimated using 1-D averaged stacking velocity models. These velocities were consistent with downhole measurements for central Utah.

The datasets for three seismic profiles are capable of producing coherent reflection images in which structure at depth can be interpreted. Line 2, adjacent to the Green River, spans an area near a recent scientific borehole CO2 W55 which provides an assist for determining contact depths for the Entrada, Carmel, and Navajo Formations. Anticlines that may behave as traps for CO2 gas are discernable as well and give some insight into the flow pathways of CO2 to the surface.

Line 2

The scientific borehole CO2 W55 was drilled on the foot wall of the LGWF ~50 m west of the Line 2 profile (Figure 2.2). The Line 2 reflection image (Figure 3.12) shows coherent reflectors near the inferred top and bottom boundaries of the Navajo Sandstone as well as the lower contact of the Entrada Sandstone at 149 m depth (Kampman et al., 2014). Lateral changes in reflection amplitude support the fault location observed as a slow Vp zone from the Line 2 tomogram. The LGWF crosses the Green River anticline (Figure 2.1), as mapped by Doelling et al. (2015). The intersection of the anticline with the east-west trending LGWF creates a structural trap for up flowing CO2 (Naruk 2019).

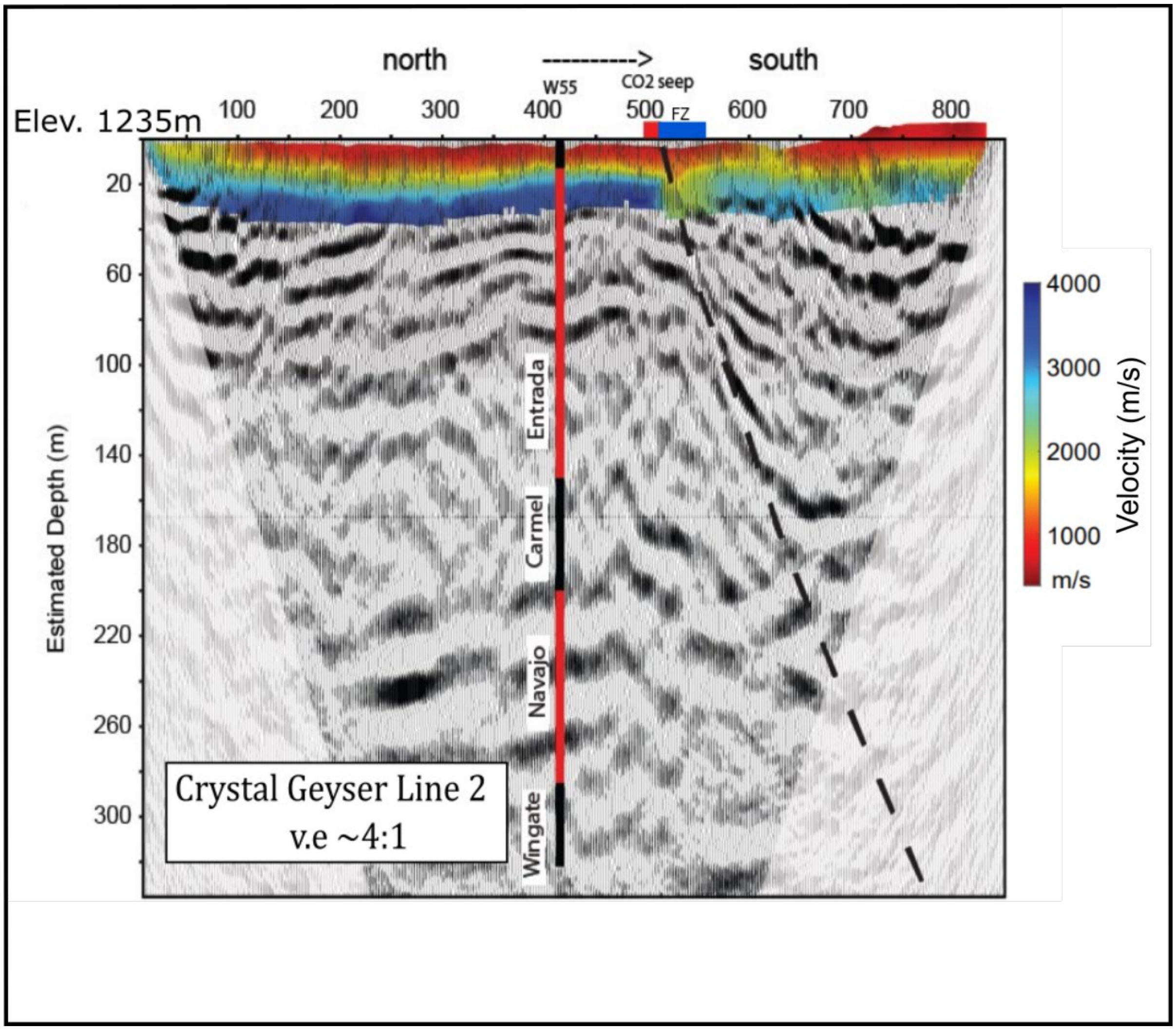

Figure 3.12 Reflection image for Line 2 at 4:1 vertical exaggeration with overlain refraction tomogram and borehole log from CO2 W55.

Line 3

The Line 3 reflection profile crosses the LGWF on the northern end and mostly consists of the hanging wall of the LGWF (Figure 3.14). The crest of an anticline mapped by Doelling et al. 2015 can be seen by curvature of reflections near the southern end of the profile. Offset reflectors near position 5500 is consistent with a near vertical fault.

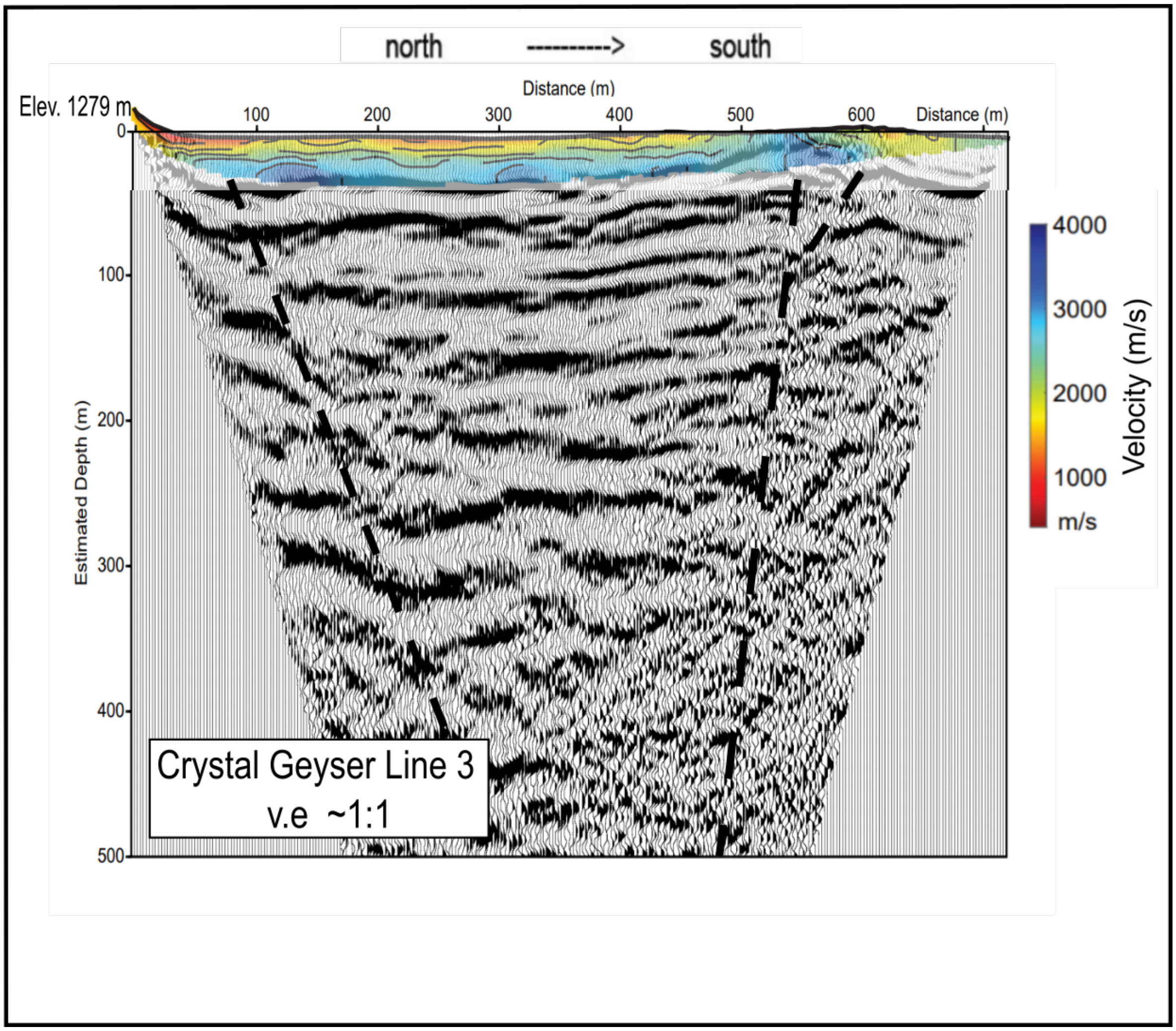

Figure 3.13 Line 3 reflection image at 1:1 vertical exaggeration with overlain line 3 refraction tomogram.

Line 7

I processed the dataset of Line 7 to produce a reflection image with 4:1 vertical exaggeration (Figure 3.9). The dramatic change in reflection amplitude laterally at 300-340 m along the profile indicates the location and architecture of the LGWF at depth. The strong reflection seen south of the fault compared to weaker reflections north of the fault may be representative of the large amount of fault throw previously described in the is span of the fault (Kampman et al. 2014b).

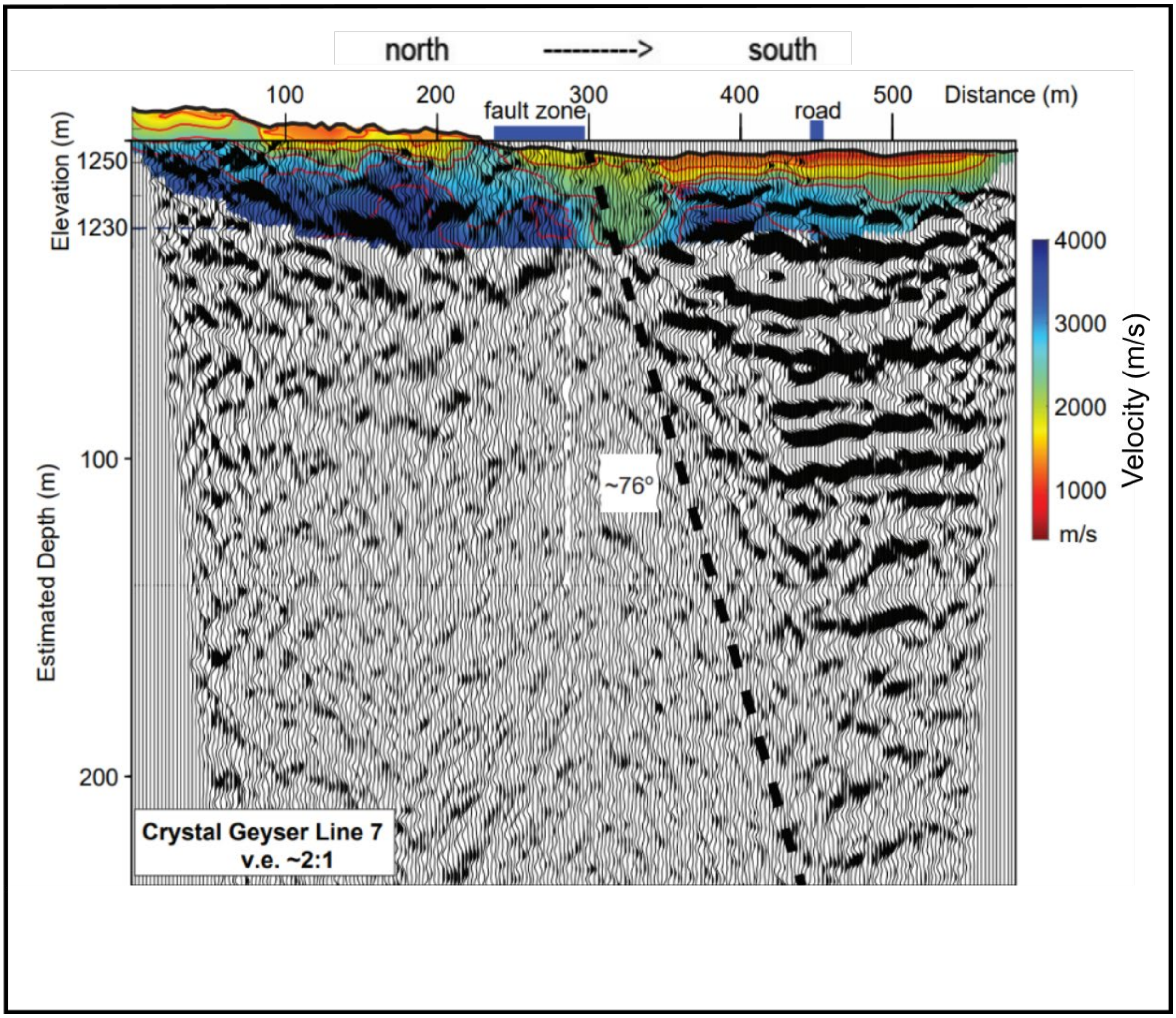

Figure 3.14 Line 7 reflection image at 1:1 vertical exaggeration with overlain Line 7 Vp refraction tomogram.

CHAPTER FOUR: DISCUSSION

My dataset provides an ideal seismic velocity comparison to lithology, to mapped fault locations, to measured CO2 flux rates, to elevations, and to ancient CO2 pathways. Here, I focus on seismic velocity distributions in the upper 20 to 40 m. I focus on a comparison of seismic velocities to lithology, estimated porosity, fluid saturation, and the presence of modern and relic CO2 pathways to the surface. I use seismic reflection images to place the shallow velocities in a structural and stratigraphic context.

From rock chemistry from borehole CO2 W55 cores, Kampman et al. (2014) concluded that CO2-undersaturated meteoric groundwater recharges from the San Rafael Swell and flows laterally southeastward within the aquifers. Free CO2 sourced from deep reservoirs interacts in the Navajo and Entrada Sandstone CO2-charging the aquifers. The LGWF is thought to impede a lateral flow of CO2-rich brine in the aquifers but be open to upwards-directed, along-fault flow via fractures in the fault damage zone (Jung, 2014, Dockrill and Shipton 2010). The majority of CO2 outgassed within the central span of the LGWF by Jung (2014). I observe that the previously mapped northern fault traces often are not distinguishable in my tomograms. I speculate that due to buoyant fluid and gas surpassing the northern trace and being trapped by the southern fault trace and the southern mapped trace in my tomograms may more consistently align with observed zones of increased estimated porosity and V_p reduction for this reason. This would indicate that advection is the dominant process that drives CO2 migration. The lack of seismic evidence of the northern fault strand and high CO2 measurements of outgassing on the footwall may suggest some diffusive flow is also present.

Using the relationship of dependence of Vp and Vs on ϕ and V_{cl} (Equation 1-3), I estimate ϕ for each of my tomograms based on Vp and assuming a constant clay content. This provides relative porosity values for interpreting lithology and fault location. Within interpreted fault zones I observe porosity values changed +/-5-10% compared to surrounding values. This Vp to ϕ relationship, and the ϕ to permeability relationships for sandstones, suggests then that seismic velocity can be used to identify high permeability CO2 outgassing zones. Areas of slower velocity are interpreted as zones of higher porosity however this also be indicated as higher clay content. Ridgley and Hatch, (2013) found the range of porosity of 22 to 25% from for Entrada Sandstone reservoir rock. Antonellini and Aydin (1994) measured porosity in the Moab member of the Entrada Sandstone, the top 20 to 40 m directly underlying the Morrison Formation, to vary from 4 to 28%. From this range I suggest depth to bedrock relates to porosity values of 25 to 30% (0.25 to 0.3 on plots).

I interpret Vp greater than 1500 m/s to indicate saturated soil or more competent rock. Below the 1500 m/s contour, I interpret unsaturated, unconsolidated sediments. Based on this relationship, I interpret Lines 2, 3, 6 and 7 to be saturated to less than 10m depth. I speculate that Line 5 is likely unsaturated in the top 10-20 m due to a 20 to 34% decrease in Vp for the upper 25m depth when compared to other profiles. With water saturation, Vp increases, but Vs decreases slightly. However, neither P- nor S-wave velocity is the best indicator of any fluid saturation effect because of the coupling between P- and S-waves through the shear modulus and bulk density (Figure 1.2) (Han et al., 2004). As Vs is relatively insensitive to saturation, using the ratio of Vp to Vs on Line 7 can improve the estimate of saturation when compared to Vp or Vs alone. I use a ratio above 2.5 to interpret saturated areas along Line 7.

Stress acting on the fault can further open pre-existing fractures and decrease particle to particle contact. This pressure acts to increase average porosity and create more permeable pathways for fluid and gas flow (Naruk et al., 2019). I speculate the slow Vp zones observed in lines 2, 6 and 7 to be resultant of pre-existing fractures near the fault being further opened by the pressure from outflowing fluid and CO_2 gas. I speculate that high levels of CO_2 outgassing, as measured by Jung, (2014), correlate with the location of fault traces or areas north of the northern fault trace. Profiles with less CO_2 measured such as Lines 5 and 6 show a weaker link between CO_2 outgassing and fault location when compared to Lines 2 and 7. Here, higher measured CO_2 flux show the highest levels of outgassing near mapped fault traces.

Conclusion

For the successful long-term storage of CO_2, it is essential to determine how existing faults will behave when introducing pressurized fluid. Determining whether a fault will act as a conduit or barrier for flowing material will greatly affect the viability of a storage system. Understanding the dynamics of CCS is critical to identification of potential leakage pathways or active leaking of a storage system.

Through seismic imaging I show low velocity zones that relate to high permeability, high CO_2 flux zones. The width of interpreted damage zones within the fault are interpreted to be greater than have been previously documented. A significant reduction in seismic velocity is observable at all depths across the LGWF in first arrival tomograms. Places along the fault at which I observe slow velocities show high levels of CO_2 flux (Jung et al. 2014). It is possible CO_2 gas present in the rock pore space creates pressure to offset the effective stress on the fault, opening pre-existing fractures in the fault.

My findings can be applied to other CCS sites to identify outgassing CO_2. Seismic velocity can be used to estimate porosity, to find high porosity zones and to identify potential high permeability CO_2 outgassing zones. CO_2 within a fault to the surface can be identified via hammer seismic survey and manifests as slow velocity zones. The ability to identify pathways of leaking CO_2 via seismic methods offers a low-cost monitoring strategy for CCS sites. Additional data that would improve my approach are regularly spaced and temporal CO_2 concentration measurements that are tied to the geyser eruption cycle. Time-lapse seismic to image the sandstone aquifers through an eruption cycle would help understand how material in the aquifer migrates as pressure rises and falls.

REFERENCES

Assayag, N., Bickle, M., Kampman, N., Becker, J., 2009. Carbon isotopic constraints on CO2 degassing in cold-water Geysers, Green River, Utah. Energy Procedia 1 (1), 2361–2366.\

Baer, James L., and Rigby, J. Keith, 1978, Geology of the Crystal Geyser and environmental implications of its effluent, Grand County, Utah: Utah Geology, v.5, no. 2, p. 125-130.

Brantut, N., & David, E. C. (2018). Influence of fluids on VP/VS ratio: increase or decrease? Geophysical Journal International, 216(3), 2037–2043. https://doi.org/10.1093/gji/ggy518

Brocher, T. M. (2005). Empirical relations between elastic wavespeeds and density in the Earth's crust. Bulletin of the seismological Society of America, 95(6), 2081-2092.

Burnside, N. M. (2013). U-Th dating of travertine on the Colorado Plateau: Implications for the leakage of geologically stored CO2. PhD Thesis, University of Glasgow, i-iii.

Bourbié, T., Coussy, O., & Zinszner, B. (1987). Acoustics of porous media. Houston, TX: Gulf Publishing Company.

Caine, J. S., J. P. Evans, and C. B. Forster, 1996, Fault zone architecture and permeability structure: Geology, v. 24, no. 11, p. 1025–1028, doi:10.1130/0091-7613(1996) 0242.3.CO;2.

Castagna, J. P., Batzle, M. L., & Eastwood, R. L. (1985). Relationships between compressional-wave and shear-wave velocities in clastic silicate rocks. geophysics, 50(4), 571-581.

Chong Zeng, J. X. (2012). Numerical investigation of MASW applications in presence of surface topography. Journal of Applied Geophysics, 52-60.

Chu, S. (2009). Carbon capture and sequestration.

Clarke, B. A., & Burbank, D. W. (2011). Quantifying bedrock-fracture patterns within the shallow subsurface: Implications for rock mass strength, bedrock landslides, and erodibility. Journal of Geophysical Research: Earth Surface, 116(F4).

Dejam, M., Hassanzadeh, H., Diffusive leakage of brine from aquifers during CO2 geological storage, Advances in Water Resources, Volume 111, 2018, Pages 36-57, ISSN 0309-1708, https://doi.org/10.1016/j.advwatres.2017.10.029.

Doelling, H. H., Kuehne, P. A., Willis, G. C., & Ehler, J. B. (2015). Geologic map of the San Rafael Desert 30'x 60'quadrangle, Emery and Grand Counties, Utah. Utah Geological Survey.

Dockrill, B., Shipton, Z.K., 2010. Structural controls on leakage from a natural CO2 geologic storage site: Central Utah, U.S.A. J. Struct. Geol. 32 (11), 1768–1782.

Faulkner, D. R., Jackson, C. A. L., Lunn, R. J., Schlische, R. W., Shipton, Z. K., Wibberley, C. A. J., & Withjack, M. O. (2010). A review of recent developments concerning the structure, mechanics and fluid flow properties of fault zones. Journal of Structural Geology, 32(11), 1557-1575.

Gettemy, G. L., Tobin, H. J., Hole, J. A., and Sayed, A. Y. (2004), Multi-scale compressional wave velocity structure of the San Gregorio Fault zone, Geophys. Res. Lett., 31, L06601, doi:10.1029/2003GL018826.

Han, D. H., & Batzle, M. L. (2004). Gassmann's equation and fluid-saturation effects on seismic velocities. Geophysics, 69(2), 398-405.

Han, W. S., M. Lu, B. J. Mcpherson, E. H. Keating, J. Moore, E. Park, Z. T. Watson, and N. H. Jung, 2013, Characteristics of CO2-driven cold-water geyser, Crystal Geyser in Utah: Experimental observation and mechanism analyses: Geofluids, v. 13, no. 3, p. 283–297, doi:10.1111/gfl.12018.

Heath, J. E., Lachmar, T. E., Evans, J. P., Kolesar, P. T., Williams, A. P., McPherson, B. J., & Sundquist, E. T. (2009). Hydrogeochemical characterization of leaking, carbon dioxide-charged fault zones in east-central Utah, with implications for geologic carbon storage. Carbon sequestration and its role in the global carbon cycle, 183, 147-158.

Jianghai Xia, R. D. (1999). Estimation of near-surface shear-wave velocity by inversion of Rayleigh waves. Geophysics, 691-700.

Jongwook Kim, T. M. (2011). Monitoring and detecting CO2 injected into water-saturated sandstone with joint seismic and resistivity measurements. Exploration Geophysics, 42:1, 58-68, DOI: 10.1071/EG11002.

Jung, N. (2014). Fault-controlled advective, diffusive, and eruptive CO0RW1S34RfeSDcfkexd09rT4 21RW1S34RfeSDcfkexd09rT4 leakage from natural reservoirs in the colorado plateau, east-central utah (Order No. 1573347). Available from ProQuest Dissertations & Theses Global. (1651982087).

Kampman, N., M. J. Bickle, M. Wigley, and B. Dubacq, 2014b, Fluid flow and CO2–fluid–mineral interactions during CO2-storage in sedimentary basins: Chemical Geology, v. 369, p. 22–50, doi:10.1016/j.chemgeo.2013.11.012.

Keleman, P., Benson, S. M., Pilorge, H., Psarras, P., & Wilcox, J. (2019, November 15). An Overview of the Status and Challenges of CO2 Storage in Minerals and Geological Formations. Frontiers in Climate.

Lee, M. W. (2003). Velocity ratio and its application to predicting velocities. US Department of the Interior, US Geological Survey.

Liberty, L. M., St. Clair, J., & McKean, A. P. (2021). A Broad, Distributed Active Fault Zone Lies beneath Salt Lake City, Utah. The Seismic Record, 1(1), 35-45.

Lindsey, R. (2020, August 14). Climate change: Atmospheric Carbon Dioxide: NOAA Climate.gov. Retrieved March 25, 2021, from https://www.climate.gov/news-features/understanding-climate/climate-change-atmospheric-carbon-dioxide#:~:text=Global%20atmospheric%20carbon%20dioxide%20was,%C2%B1%200.1%20ppm%20per%20year.

Mavko, G., Mukerji, T., & Dvorkin, J. (2020). The rock physics handbook. Cambridge: Cambridge University Press.

Moser, T. J. (1991). Shortest path calculation of seismic rays. Geophysics, 56(1), 59-67.

Nakatsuka, Y. (2009, February). Experimental study on monitoring and quantifying of injected CO2. Energy Procedia, Volume 1, Issue 1. Elsevier.

Nakatsuka, Y. (2010, March). Experimental study on CO2 monitoring and quantification of stored CO2 in saline formations using resistivity measurements. International Journal of Greenhouse Gas Control, Volume 4, Issue 2. Elsevier.

Naruk, S. J., Solum, J. G., Brandenburg, J. P., Origo, P., & Wolf, D. E. (2019). Effective stress constraints on vertical flow in fault zones: Learnings from natural CO 2 reservoirs. AAPG Bulletin, 103(8), 1979-2008.

Nuccio, V. F., and S. M. Condon, 1996, Burial and thermal history of the Paradox Basin, Utah and Colorado, and petroleum potential of the Middle Pennsylvanian Paradox Formation, in A. C. Huffman Jr., W. R. Lund, and L. H. Godwin, eds., Geology of the Paradox Basin: Salt Lake City, Utah, Utah Geological Association Publication 25, p. 57–76.

O'Neill, B. C., Tebaldi, C., van Vuuren, D. P., Eyring, V., Friedlingstein, P., Hurtt, G., Knutti, R., Kriegler, E., Lamarque, J.-F., Lowe, J., Meehl, G. A., Moss, R., Riahi, K., & Sanderson, B. M. (2016). The Scenario Model Intercomparison Project (ScenarioMIP) for CMIP6. Geoscientific Model Development, 9(9), 3461–3482. https://doi.org/10.5194/gmd-9-3461-2016.

Oye, Volker and Anell, Ingrid and Braathen, Alvar and Dichiarante, Anna Maria and Evans, Jim and Hafner, Alison and Liberty, Lee and Midtkandal, Ivar and Petrie, Elizabeth and Sauvin, Guillaume and Skurtveit, Elin and Yelton, Jonathan and Zuchuat, Valentin, Monitoring and imaging of active and passive CO2 seepage patterns (March 1, 2021). Proceedings of the 15th Greenhouse Gas Control Technologies Conference 15-18 March 2021, Available at SSRN: https://ssrn.com/abstract=3819197 or http://dx.doi.org/10.2139/ssrn.3819197

Rahman, F. A., Aziz, M. M. A., Saidur, R., Bakar, W. A. W. A., Hainin, M. R., Putrajaya, R., & Hassan, N. A. (2017). Pollution to solution: Capture and sequestration of carbon dioxide (CO_2) and its utilization as a renewable energy source for a sustainable future. Renewable and Sustainable Energy Reviews, 71, 112-126.

Ridgley, J. L., & Hatch, J. R. (2013). Geology and oil and gas assessment of the Todilto Total Petroleum System, San Juan Basin Province, New Mexico and Colorado: Chapter 3 in Total petroleum systems and geologic assessment of undiscovered oil and gas resources in the San Juan Basin Province, exclusive of Paleozoic rocks, New Mexico and Colorado (No. 69-F-3). US Geological Survey.

Schuster, G. T., Li, J., Lu, K., Metwally, A., AlTheyab, A., & Hanafy, S. (2017). Opportunities and pitfalls in surface-wave interpretation. Interpretation, 5(1), T131-T141.

Shipton, Z., Evans, J., Kirchner, D., Kolesar, P., Williams, A., & and Heath, J. (2004). Analysis of CO_2 leakage through "low-permeability" faults from natural. Baines, S. J. & Worden, R. H. (eds.) Geological Storage of Carbon Dioxide. Geological Society, London, Special Publications 233, 43-58.

St. Clair J. 2015. Geophysical investigations of underplating at the Middle American Trench, weathering in the critical zone, and snow water equivalent in seasonal snow, Ph.D. Dissertation, University of Wyoming, Wyoming.

Wilkenson, M., Gilfillan, S., Haszeldine, S., & Ballentine, C. J. (2009). Plumbing the Depths: testing natural tracers of subsurface CO_2 origin and leakage, Utah, USA. In M. Grobe, J. C. Pashin, & R. L. Dodge (Eds.), Carbon dioxide sequestration in geological media - State of the science (Vol. 59, pp. 619). AAPG Studies in Geology.

H. Yamabe, T. Tsuji, Y. Liang, T. Matsuoka, Influence of fluid displacement patterns on seismic velocity during supercritical CO_2 injection: simulation study for evaluation of the relationship between seismic velocity and CO_2 saturation, Int. J. Greenh. Gas Control, 46 (2016), pp. 197-204.

Yilmaz, Ö. (2001). Seismic Data Analysis. Society of Exploration Geophysicists, Volume 1. https://doi.org/10.1190/1.9781560801580